

Cold fronts in galaxy clusters^{*}

S. Ghizzardi, M. Rossetti, and S. Molendi

INAF, Istituto di Astrofisica Spaziale e Fisica Cosmica, via E. Bassini 15, 20133 Milano, Italy
e-mail: simona@iasf-milano.inaf.it

Received 14 May 2009 / Accepted 1 March 2010

ABSTRACT

Context. Cold fronts have been observed in several galaxy clusters. Understanding their nature and origin is extremely important for investigating the internal dynamics of clusters.

Aims. To gain insight into the nature of these features, we carry out a statistical investigation of their occurrence in a sample of galaxy clusters observed with XMM-Newton and correlate this occurrence with different cluster properties.

Methods. We selected a sample of 45 clusters starting from the B55 flux limited sample (Edge et al. 1990, MNRAS, 245, 559) and performed a systematic search for cold fronts.

Results. We find that a large fraction of clusters host at least one cold front. Cold fronts are easily detected in all systems that are manifestly undergoing a merger event in the plane of the sky, while the presence of these features in the remaining clusters is related to a steep entropy gradient, in agreement with theoretical expectations. Assuming that cold fronts in cool core clusters are triggered by minor merger events, we estimate a minimum of 1/3 merging events per halo per Gyr.

Key words. galaxies: clusters: general – X-rays: galaxies: clusters

1. Introduction

The unprecedented angular resolution of the X-ray telescope *Chandra* led to the discovery of several new phenomena within various astrophysical systems. One of these are cold fronts detected in galaxy clusters. Initially observed in merging clusters, the prototypes are found in A2142 (Markevitch et al. 2000), A3667 (Vikhlinin et al. 2001a,b; Vikhlinin & Markevitch 2002), and 1E0657-56 (Markevitch et al. 2002). All these systems feature very sharp discontinuities in their X-ray images where the drop of the surface brightness (and correspondingly of the gas density) is accompanied by a jump in the gas temperature, with the denser region colder than the more rarefied region, unlike in shock fronts. For this reason, these features have been dubbed “cold fronts” (Vikhlinin et al. 2001a). The density and the temperature discontinuities have similar amplitudes so that pressure is approximatively continuous across the front. Cold fronts have been initially interpreted as the edge of the cool core of a merging substructure that has survived the merger and is rapidly moving through the ambient gas (Markevitch et al. 2000).

Cold fronts have been successively detected in the cores of some relaxed clusters (e.g. A1795: Markevitch et al. 2001; RX J1720.1+2638: Mazzotta et al. 2001; A496: Dupke & White 2003; 2A 0335+096: Mazzotta et al. 2003), and to date a large number of relaxed systems are known to host one. Since the presence of cold fronts in cool cores provides evidence of gas motions and possibly of departures from hydrostatic equilibrium, understanding the nature of such a widespread phenomenon is mandatory for characterizing the dynamics of galaxy clusters. High-resolution hydrodynamical simulations are, at present, the main technique for investigating the mechanisms generating cold fronts. Indeed, cold front features could already be detected in simulations published prior to the launch of *Chandra*

(Roettiger et al. 1997, 1998). After cold fronts had been discovered, several hydrodynamical simulations were developed to model the effect of the ram-pressure stripping during a merger event and the formation of the cold front feature in merging clusters (Heinz et al. 2003; Nagai & Kravtsov 2003; Mathis et al. 2005). Several simulations have also been employed to understand the origin of cold fronts in relaxed non-merging clusters (e.g. Churazov et al. 2003; Tittley & Henriksen 2005; Ascasibar & Markevitch 2006).

The emerging picture (Ascasibar & Markevitch 2006; see also Markevitch & Vikhlinin 2007, for a review) is that cold fronts arise during major merging events through ram-pressure stripping mechanisms that induce the discontinuity among the merging dense subcluster and the less dense surrounding ICM. In relaxed clusters, the cold fronts features are induced by minor merger events that produce a disturbance on the gas in the core, displace it from the center of the potential well, and decouple it from the underlying dark matter through ram pressure. Subsequently, a sloshing mechanism sets in, generating cold fronts. The necessary condition for triggering this mechanism is the steep entropy profile for the central gas that is generally fulfilled at the center of relaxed cool core clusters.

Cold fronts are at present observed in several galaxy clusters. Markevitch et al. (2003) analyzed a sample of 37 relaxed clusters observed with *Chandra*, showing that cold fronts are present in the majority of the cores of relaxed clusters. Recently, Owers et al. (2009) have characterized a sample of nine cold fronts with quantitative measurements of the thermodynamic discontinuities across the edges and associated the cold front with evidence of merger activity.

While many objects have been studied in detail to understand the nature of cold fronts, we still lack a systematic investigation of the characteristics of these phenomena and of their host clusters through a large sample. The aim of this paper is to perform a systematic search of cold fronts in a representative

^{*} Appendix is only available in electronic form at <http://www.aanda.org>

sample and to investigate the properties of their parent clusters. Such a study is needed to inspect the nature and origin of cold fronts and eventually to test the reliability of the picture emerging from the simulations.

The sample was selected starting from the B55 flux-limited sample by [Edge et al. \(1990\)](#). We used *XMM-Newton* data for our analysis. In spite of its limited spatial resolution with respect to *Chandra*, *XMM-Newton* has the positive attribute of having a large field of view, thereby allowing a significant coverage of most of the clusters. In most cases, the clusters are inside the EPIC field of view up to a radius $\gtrsim 0.3 r_{180}$, allowing the characterization of the main thermodynamical properties well beyond the core regions. Additionally, the *XMM-Newton* large collecting area allows good statistics for a large number of objects.

Among the several physical properties characterizing the intracluster medium, we focus our attention on entropy. Entropy plays a key role in describing the thermodynamical state of the ICM, its distribution is a signature of the thermodynamical history of the cluster, and it is also intimately related to the non-gravitational processes that may have occurred ([Voit et al. 2002, 2005](#)). Moreover, as previously stressed, simulations highlight how the steep gas entropy profile is a necessary condition for the onset of the sloshing mechanism and therefore for the presence of cold fronts in cool core clusters ([Ascasibar & Markevitch 2006](#)).

The structure of the paper is the following. In Sect. 2 we describe the sample of clusters we analyzed, and in Sect. 3 we provide details about the data reduction. Then we describe (see Sect. 4) the algorithm used for the systematic search of cold fronts in the cluster sample. We present our results about the occurrence and the origin of cold fronts in Sect. 5 and discuss them in Sect. 6. We summarize our findings in Sect. 7.

We adopt a Λ CDM cosmology with $\Omega_m = 0.3$, $\Omega_\Lambda = 0.7$, and $H_0 = 70 \text{ km s}^{-1} \text{ Mpc}^{-1}$.

2. The sample

We used the flux-limited sample by [Edge et al. \(1990\)](#) as a reference starting sample. It includes 55 objects with flux $f_x > 1.7 \times 10^{-11} \text{ erg cm}^{-2} \text{ s}^{-1}$ in the 2–10 keV energy band and is 90% complete. All the clusters are located at redshift $z < 0.2$.

Starting from this sample, we selected all the clusters available in the *XMM-Newton* public archive. At the time of writing, Ophiuchus was not publicly available and the objects A2244 and A644 had not been observed with *XMM-Newton*. For A754 we used the long observations we obtained from AO7 (P.I.: A. Leccardi). Observations for 3C129, A2142, A2147, A1736, and A3391 are highly affected by soft protons. Since their final good exposure time after cleaning procedures is generally below 5 ks for MOS and < 0.5 ks for *pn*, these clusters were excised from the sample. For clusters with more than one observation, we eliminated those observations with high soft protons contamination. We also excluded Virgo and Coma, because their extension does not allow significant coverage within the EPIC field of view.

Our final sample is reduced to 45 objects. In Table 1 we filed the list of clusters belonging to our sample. The excision of several clusters invalidates the completeness of the sample. To verify that the final sample is representative of the cluster population, we inspected the distribution of the main cluster observables. We built the histograms for redshift, X-ray luminosity, and temperature (see Fig. 1) both for the starting sample (light grey) and for the excluded clusters (dark grey). For X-ray luminosities (L_x), we refer to [Reiprich & Böhringer \(2002\)](#),

Table 1. The list of the 45 clusters belonging to our sample.

Cluster name	Redshift	Cluster name	Redshift
Centaurus	0.0114	A85	0.0551
A1060	0.0126	A3532	0.0554
A262	0.0163	A3667	0.0556
AWM7	0.0172	A2319	0.0557
Perseus	0.0176	Cygnus A	0.0561
A1367	0.0220	A2256	0.0581
A4038	0.0300	A3266	0.0589
A2199	0.0302	A3158	0.0597
A496	0.0329	A1795	0.0625
2A0335	0.0349	A399	0.0718
A2063	0.0349	A2065	0.0726
A2052	0.0355	A401	0.0737
A576	0.0389	A3112	0.0750
A3571	0.0391	A2029	0.0773
A119	0.0442	A2255	0.0806
MKW3s	0.0450	A1650	0.0838
A1644	0.0473	A1651	0.0849
A4059	0.0475	A2597	0.0852
A3558	0.0480	A478	0.0881
A3562	0.0490	PKS0745	0.1028
Triang. Aus.	0.0510	A2204	0.1523
Hydra A	0.0538	A1689	0.1832
A754	0.0542		

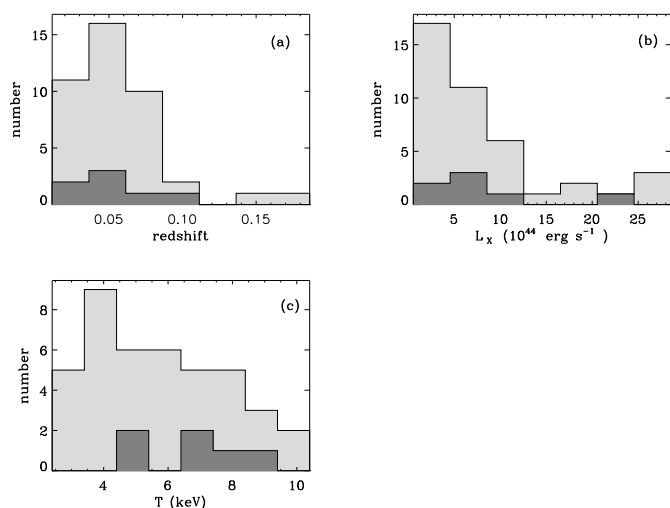


Fig. 1. Distributions of redshifts **a**), X-ray luminosities **b**), and temperatures **c**) for the starting ([Edge et al. 1990](#); [Peres et al. 1998](#)) clusters sample (light grey) and for the excised objects (dark grey). The rejection of these objects does not introduce any obvious bias on the remaining subsample.

while temperatures were taken from [Peres et al. \(1998\)](#). The histograms show that excluded clusters do not introduce any obvious bias. We conclude that, even if the final adopted sample is not complete, it is representative of the cluster population.

3. Data reduction

Observation Data Files (ODF) were retrieved from the *XMM-Newton* archive and processed in a standard way with the Science Analysis System (SAS) v6.1. We applied the standard selection `#XMMEA_EM` to the MOS event list (`#XMMEA_EP` for *pn*) to automatically filter out artefact events. The soft protons cleaning was performed using a double filtering process (see [Leccardi & Molendi 2008](#); [Pratt & Arnaud 2002](#)). The

adoption of a threshold level and the exclusion of light curve intervals above the selected threshold allows rejection of most flare events. In practice, we extracted the light curve in the 10–12 keV (10–13 keV) energy band for MOS (*pn*) using 100 s bins. We applied a threshold of 0.20 cts s⁻¹ for MOS and 0.50 cts s⁻¹ for *pn* to generate the filtered event file. However softer flares may exist such that their contribution above 10 keV is negligible. To remove this flare contamination, we applied the 3 σ clipping method (see Marty et al. 2003): we extracted a histogram of the light curve in the 2–5 keV band and fit this histogram with a Gaussian distribution. Since most flares had already been rejected in the previous step, the fit was usually very good. We then applied a threshold at the +3 σ level and generate the filtered event file. After soft proton cleaning, we filtered the event file according to FLAG (FLAG=0) and PATTERN criteria (PATTERN \leq 12).

To systematically search surface brightness discontinuities, for each cluster, we built the EPIC flux map: MOS1 + MOS2 + *pn* (*pn* images are corrected for out of time events). This flux image was computed in the 0.4–2 keV band following a procedure similar to the one described in Baldi et al. (2002, see also Rossetti et al. 2007). We summed up the MOS1, MOS2, and *pn* source images to obtain the total source map, S_{EPIC} , and we computed EPIC source exposure map, exp_{EPIC} , by summing the source exposure maps of each detector. The EPIC count rate image was then defined as $cr_{\text{EPIC}} = S_{\text{EPIC}} / \text{exp}_{\text{EPIC}}$. Count rates were then converted to flux through the total conversion factor cf_{EPIC} derived following the formula:

$$\frac{\text{exp}_{\text{EPIC}}}{cf_{\text{EPIC}}} = \frac{\text{exp}_{\text{MOS1}}}{cf_{\text{MOS1}}} + \frac{\text{exp}_{\text{MOS2}}}{cf_{\text{MOS2}}} + \frac{\text{exp}_{\text{pn}}}{cf_{\text{pn}}}$$

where cf_{MOS1} , cf_{MOS2} , cf_{pn} and exp_{MOS1} , exp_{MOS2} , exp_{pn} are the conversion factors and the exposure maps of the three instruments. The EPIC source flux image was obtained using the relation $f_{\text{EPIC}} = cf_{\text{EPIC}} \cdot cr_{\text{EPIC}}$.

To remove the quiescent particle induced background and the cosmic background component, we need EPIC background flux images. We used a large collection of background data, such as long observations of blank sky fields. We used 9 blank fields (for a total exposure time of \sim 300 ks) selected by our own group (Leccardi & Molendi 2008). We computed the EPIC background flux image from the MOS1, MOS2, and *pn* background images and exposure maps using the same method applied to the EPIC source flux image. By subtracting the EPIC background flux image from the source flux image, we derived an EPIC net flux image in units of 10⁻¹⁵ erg cm⁻² s⁻¹ pixel⁻¹ (one pixel is 8.5 \times 8.5 arcsec²). The net maps were used for the construction of the surface brightness profiles.

To search for cold fronts, we also need the temperature maps of all the clusters of our sample. We adopted a modified version of the “adaptive binning + Broad Band Fitting” algorithm described in Rossetti et al. (2007), where we substituted the Cappellari & Copin (2003) adaptive binning algorithm by its modified version by Diehl & Statler (2006).

4. Systematic search of cold fronts

4.1. The detection algorithm

In this section, we identify a suitable method of detecting cold fronts, well aware that any general selection criterion will have some limitations and can introduce spurious effects, so that some cold fronts may be missed and some features may be classified

as cold fronts although they are not. We address this point in detail in Sects. 4.2 and 5.1.

A cold front is characterized by the presence of a sharp decrease in the surface brightness (*SB*) profile typically accompanied by a rise in the gas temperature. We initially perform a systematic search of surface brightness discontinuities in the cluster sample and generate a list of candidate cold fronts. Subsequently, we examine the gas temperature behavior across the discontinuity, to rule out the hypothesis that the detected discontinuity is a shock front.

We have developed an algorithm to perform the systematic search of surface brightness discontinuities. We start from the EPIC flux maps (see Sect. 3) that we built for our sample, and we divide each cluster map in 30 $^\circ$ wide sectors centered on the *SB* peak. In most cases, we detected *SB* discontinuities in several consecutive sectors, suggesting that most cold fronts have an angular extension significantly larger than 30 $^\circ$. Consequently, unless the statistics is particularly low, fixed angular ranges can be used to find discontinuities. A possible bias on the detectability of cold fronts due to the width of the angular sectors will be discussed in Sect. 5. For clusters with a low statistics or where the possible cold front is located near the cluster center (e.g. A262, A1795, A2199), we use an “ad hoc” choice of the sectors (45 $^\circ$ wide or even larger) to reveal the discontinuity in the surface brightness profiles. We build the surface brightness profile for each sector using the cluster X-ray emission peak as center. Sometimes, for merging or irregular clusters, a visual inspection of the images may suggest a different center, better suited to detecting a sharp decrease in the surface brightness. As an example, in Fig. 2 we show the surface brightness images of A2319 and A1367 with the centers adopted to build the profiles.

For each cluster a set of profiles is obtained. While for some clusters (e.g. Centaurus, A496, 2A0335+096) the presence of a surface brightness discontinuity is apparent, in other clusters (e.g. A262) the surface brightness profile is not as sharp (see Fig. 3). Projection effects and resolution limits smooth the profiles: the surface brightness discontinuity will appear as a steepening of the profile in the radial range around the jump radius. In the approximation where profiles are described by power laws, the slopes measure the steepness of the profile. We use the power law slopes to characterize the surface brightness discontinuities. We identify, for each cluster, the possible discontinuity region (labeled with the letter D, from now on) with a visual inspection of the profile and of the image. We set $SB \propto r^{-\alpha_D}$ in the corresponding radial range (see upper-right panel of Fig. 3 as an example). We compare the slope we find in this region with the slope obtained fitting the profile with the power law $SB \propto r^{-\alpha_{ND}}$ in the nearby (inner and/or outer) region or in other sectors of the cluster where no irregularities in the surface brightness profiles are present. The difference in the slopes $\Delta\alpha = \alpha_D - \alpha_{ND}$ quantifies the steepening of the profile. We require that $\Delta\alpha \geq 0.4$ to classify a region as discontinuous. The choice of this threshold relies on phenomenological considerations. All the jumps we measured have $\Delta\alpha$ values well above 0.5, while $\Delta\alpha$ values are below 0.2 for regions without discontinuities.

Examples of different surface brightness profiles are reported in Fig. 3. Centaurus cluster profiles (top left panel in the figure) steepen significantly between 50''–100'' in the NE sector and between 170''–210'' in the W-NW sector. In A262 and in A1060 (top right panel and bottom left panel, respectively), the discontinuities are not as apparent as in Centaurus. Finally, the profile for AWM7 (bottom right panel) does not show any irregularity. We fit all the profiles in the different radial ranges with power laws. In Table 2, we report, for each region of the four clusters shown

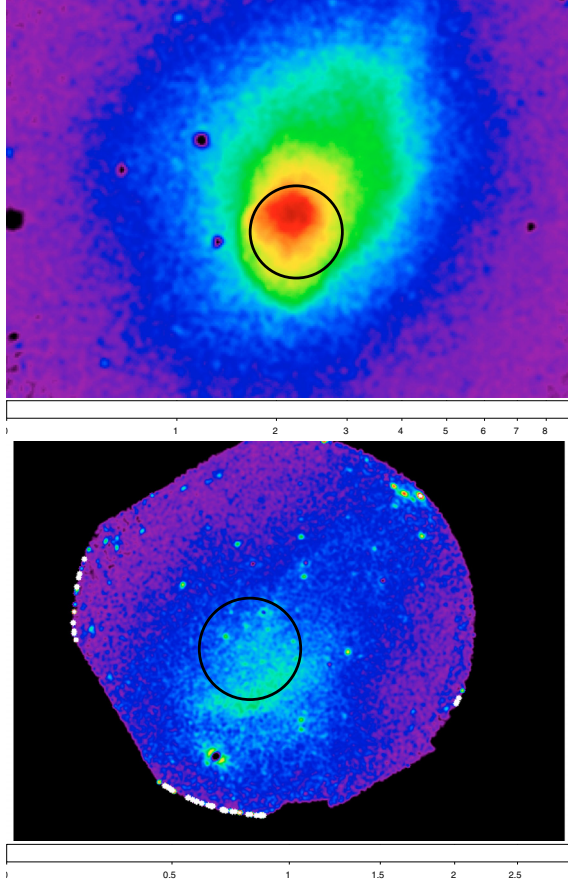


Fig. 2. Surface brightness map for A2319 (*top panel*) and A1367 (*bottom panel*). The maps have been smoothed for better visual inspection. The black circles show the position of the centers we chose for the radial profiles. They roughly match the centers of curvature of the candidate discontinuity (SE-E for A2319 and S for A1367) and do not match the X-ray emission peak. This choice allows better characterization of the jump in the surface brightness profiles.

in Fig. 3, the position angle (measured anticlockwise from east), the radial ranges used for the fits, the slopes of the best fits in the given radial range, the associated $\Delta\alpha$ values. In the last column, a flag indicates which features are classified as discontinuities.

For the Centaurus cluster, we consider two interesting sectors, SE and W-NW of the cluster core. The slopes we find for the W-NW sector (specifically, $120^\circ - 150^\circ$, where the angles are measured in an anticlockwise direction from east) are 0.41, 2.59, and 0.84 for the radial ranges: $10'' - 50''$, $50'' - 100''$, $100'' - 240''$, respectively. The $\Delta\alpha$ for the central region is 2.19 with respect to the innermost region and 1.75 with respect to the outer one. This is obviously classified as a discontinuity and is a candidate cold front. A similar analysis allows assessing that there is a discontinuity in the $170'' - 210''$ radial range in the $30^\circ - 60^\circ$ sector. The quality of the Centaurus cluster profiles is extremely high thanks to its proximity and to the long observations (170 ks in the public archive at the time of writing) so that, even at the margin of the cold front located west of the core, from -60° to 60° , the discontinuity is still visible in the profile. The $\Delta\alpha$ we find for this case, 1.60, is lower than in the previous case, but still high.

In the top right panel, we show the profile for the SW-W region ($-45^\circ - 0^\circ$) in A262, where a discontinuity at $\sim 60''$, albeit not very sharp, is identifiable ($\Delta\alpha$ is slightly smaller than 1). In A1060 (bottom left panel) the putative discontinuity is around

$2'$. As shown in Table 2, the analysis of the slopes provides $\Delta\alpha = 0.02$. As a consequence, this feature is not classified as a discontinuity. However, a different result could be obtained with a slightly different choice of the radial ranges used for the fits. If we restrict the range of the discontinuity region to $110'' - 130''$ (3 points for the fit) and choose $150'' - 250''$ for the outer region (disregarding the 4 points immediately after the discontinuity where the profile is flat), $\Delta\alpha$ increases to 0.55 and this feature could be considered as a discontinuity. We believe that this choice of the radial range is rather extreme. In addition, we note that the temperature profile shows no variations in the same region. As a general rule, if $\Delta\alpha$ satisfies the discontinuity condition for an ad hoc choice of the radial range, we exclude it from the list of candidate cold fronts. Finally, in the bottom right panel in Fig. 3, AWM7 shows a regular behavior. In the figure we report one region, but AWM7 is regular in all its sectors and all profiles are similar, so we find no discontinuities for this cluster.

The procedure described thus far detects surface brightness discontinuities and provides a list of candidate cold fronts. To upgrade a discontinuity to a cold front, we need to verify the behavior of the temperature profile across the surface brightness jump. To this aim, we build the binned temperature maps (see Sect. 3 and Rossetti et al. 2007) for all the clusters of our sample. From these maps, we derive the temperature profiles plotting all the bins whose barycenter is inside the sector hosting the surface brightness discontinuity. In none of the candidate cold fronts we observe a sharp decrease in the temperature profile as would be expected for a shock front. Almost all the surface brightness discontinuities that we find feature a sharp gas temperature rise. In some cases, the temperature rises smoothly with no jumps. We notice that the cold front feature does not necessarily require a temperature jump, since the thermal pressure of the gas inside the cold front is balanced by the sum of the thermal and ram pressures outside. This can also be achieved with a slow continuous rise of the temperature across the discontinuity.

4.2. Notes on individual clusters

In Table 3, we list the clusters hosting one or more cold fronts. For each cluster, the table provides the center used to build the SB profiles, the cold front, the radial and azimuthal position of the cold front and $\Delta\alpha$. The $\Delta\alpha$ reported for each cold front is the mean value obtained by averaging over the different sectors hosting the discontinuities.

As already pointed out, the procedure adopted for classifying cold fronts can fail to find the discontinuities or can provide some doubtful cases. As a result, comments are required for some individual systems.

- **A4059**: a visual inspection of the surface brightness map of A4059 hints to a possible cold front in the SW sector $\sim 30''$ from the peak, but the discontinuity is barely visible in the profiles, and we did not succeed in fitting it with power laws and deriving $\Delta\alpha$. We consider this as an unclassified case.
- **A85**: This object has two possible cold fronts. The former lies in the NW sector $\sim 80''$ from the X-ray peak. In this sector $\Delta\alpha = 0.75$, above our threshold. However, the sector of the cold front is very narrow (30°) and no discontinuities are detected in the nearby sectors. Table 2 shows that the cold fronts widths generally range from 60° to 120° . Such a tiny extension for a cold front is unusual, and we prefer to consider this as an unclassified case. Another cold front is present in a small subclump located $8'$ south of the cluster and moving north towards the main structure

Table 2. Cold fronts candidates for the four clusters plotted in Fig. 3.

Cluster	Position angle (deg)	Radial range (arcsec)	α	Ranges for $\Delta\alpha$	$\Delta\alpha$	Discont.
Centaurus (internal)	[120,150]	10–50	0.41			
Centaurus (external)	[120,150]	100–240	0.84			
Centaurus (possib disc)	[120,150]	50–100	2.59	$\alpha_{[50-100]} - \alpha_{[10-50]}$	2.19	✓
Centaurus (possib disc)	[120,150]	50–100	2.59	$\alpha_{[50-100]} - \alpha_{[100-240]}$	1.75	✓
Centaurus (internal)	[30,60]	10–170	0.88			
Centaurus (external)	[30,60]	210–600	1.16			
Centaurus (possib disc)	[30,60]	170–210	2.52	$\alpha_{[170-210]} - \alpha_{[210-600]}$	1.64	✓
Centaurus (possib disc)	[30,60]	170–210	2.52	$\alpha_{[170-210]} - \alpha_{[10-170]}$	1.36	✓
A262 (internal)	[−45,0]	10–38	0.84			
A262 (external)	[−45,0]	70–145	0.72			
A262 (possib disc)	[−45,0]	38–70	1.66	$\alpha_{[38-70]} - \alpha_{[10-38]}$	0.82	✓
A262 (possib disc)	[−45,0]	38–70	1.66	$\alpha_{[38-70]} - \alpha_{[70-145]}$	0.94	✓
A1060 (possib disc)	[120,150]	80–135	0.94			
A1060 (external)	[120,150]	135–250	0.92	$\alpha_{[80-135]} - \alpha_{[135-250]}$	0.02	×
AWM7	[−90,−60]	20–200	0.76		0.00	×

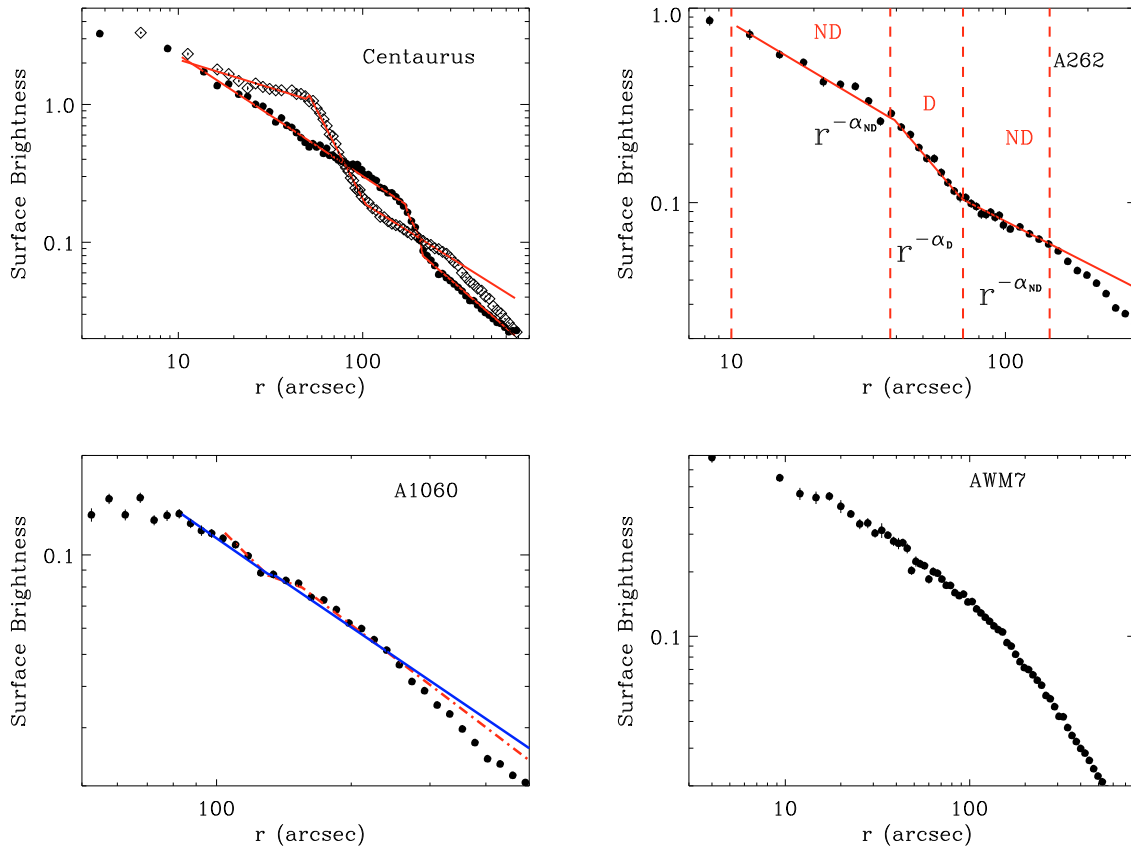


Fig. 3. Surface brightness profiles for some sectors of four clusters of our sample. For the Centaurus cluster we plot two interesting sectors: SE (filled circles) and N–NW (open diamonds) of the cluster core. The figure shows that profiles may have different behaviors. While discontinuities are apparent in some clusters (e.g. Centaurus cluster), they are not as sharp in others. Some systems (e.g. AWM7) have a regular profile. In the upper right panel (A262) we plot the ranges used to fit the profile with power laws. The flag D marks the discontinuity region and ND marks the adjacent (inner and outer) regions. In all the panels the solid lines represent power law best fits (see text and Table 2 for details). In these plots, surface brightness is given in $10^{-15} \text{ erg cm}^{-2} \text{ s}^{-1} \text{ arcsec}^{-2}$ units.

(Durret et al. 1998; Kempner et al. 2002). This is labeled as **A85*** in Table 3 to distinguish it from the unclassified cold front of the main cluster.

- **A2052:** the analysis of the discontinuities in A2052 is complex because of the bright shells surrounding the X-ray cavities (Blanton et al. 2003, 2001). Remarkably, sharp decrements of the surface brightness profiles are detected

just outside the rims, at distances of about $40''$ – $50''$ (rims are at $10''$ – $30''$ from the center). It is difficult to establish whether such sharp drops are real discontinuities or if they are associated to the bright shells. Recent results obtained from a deep *Chandra* observation (Blanton et al. 2007) show that some cavities and ripples are present in this cluster, similar to what has been observed in Perseus clusters and M87

Table 3. List of the cold fronts detected in the sample.

Cluster name	Center	Position angle (deg)	Jump radius (arcsec)	$\Delta\alpha$ (mean value)
Centaurus	12:48:49.173 -41:18:45.65	[-60, 60]	170–210	1.60
Centaurus	12:48:49.173 -41:18:45.65	[90, 210]	50–100	1.76
A262	01:52:46.117 36:09:05.79	[-110, 0]	38–70	1.06
A262	01:52:46.117 36:09:05.79	[30, 135]	40–50	1.40
Perseus	03:19:48 41:30:40	[-60, 0]	250–300	1.72
Perseus	03:19:48 41:30:40	[30, 150]	140–200	1.80
A2199	16:28:38.193 39:33:02.70	[-75, -25]	25–30	0.50
A496	04:33:38.067 -13:15:40.91	[-120, -30]	40–55	0.79
A496	04:33:38.067 -13:15:40.91	[-120, -75]	180–280	1.33
A496	04:33:38.067 -13:15:40.91	[30, 120]	80–100	1.86
2A0335+096	03:38:40.879 09:58:01.20	[-120, -30]	50–70	1.16
A1644	12:57:12.231 -17:24:32.67	[-180, -90]	20–35	1.58
A3558	13:27:56.989 -31:29:50.00	[-30, 120]	80–120	1.04
A1795	13:48:52.879 +26:35:27.80	[-130, -80]	60–70	1.14
A2065	15:22:29.455 +27:42:23.81	[-150, -90]	80–100	1.26
A576	07:21:30.495 +55:45:45.32	[-120, -60]	80–100	0.72
A3562	13:33:36.766 -31:40:20.45	[-150, -60]	60–100	1.06
A1367	11:44:53.5 19:44:19.12	[-120, -60]	350 (70 from the peak)	0.84
A754	09:09:20.098 -09:40:52.22	[120, 240]	80–150	1.14
A85*	00:41:42.733 -09:26:33.10	[0, 90]	25–80	1.40
A3667	20:12:41.653 -56:50:52.94	[-180, -90]	250–280	3.68
A2319	19:21:11.097 +43:56:08.00	[-180, -60]	100–150 (160 from the peak)	1.85
A2256	17:02:33.009 +78:38:23.59	[-135, -90]	50–75 (100 from the peak)	2.00
A3266	04:31:13.951 -61:27:26.41	[-90, -30]	60–100	0.87

Notes. Bold faced fonts mark clusters having a merging cold front while italic fonts mark clusters whose merger geometry is not clear and the origin of the cold front is not as obvious (see Sect. 5.3).

(Fabian et al. 2006, 2003; Forman et al. 2007). Some weak shocks may also be present. The presence of cold fronts is unclear so we consider this cluster as unclassified.

- **Hydra A:** in Hydra A, we detect a cold front in the 300° – 330° sector $\sim 50''$ from the core, inside the region of the weak shock at $\sim 200''$ (McNamara et al. 2005; Nulsen et al. 2005). Similar to A85, the sector of the cold front is narrow (30°). The jump is located at the bending of the south radio lobe (visible in the Hydra A radio maps at 1.4 GHz; see for example Lane et al. 2004) towards the east, near the SW cavity. In that region the temperature map shows several cold blobs, and one of this produces the temperature rise coincident with the surface brightness steepening, but no clear front in the temperature map is present. The structure of Hydra A is very complex with a strong interaction between the radio lobes and the ICM gas (Nulsen et al. 2002; McNamara et al. 2000; see also McNamara & Nulsen 2007). The cluster exhibits several cavities in the central regions (Wise et al. 2007). The discontinuity we find is probably the result of such a complicated morphology and it is probably not a cold front. Even if this region satisfies all the required conditions we consider this as an unclassified case.

Since the existence of a cold front in A2052, A4059, and Hydra A cannot be definitively established, we exclude these systems from the sample.

5. Occurrence of cold fronts

5.1. Cold fronts occurrence: a general view

The exclusion of three unclassified objects (namely A2052, A4059, Hydra A) reduces the sample to 42 objects of which 19 host a cold front, corresponding to a fraction of 0.45. The cold

front in the A85 subcluster (dubbed A85*) is included. The list of the detected cold fronts, with their main properties, is filed in Table 3. For each cluster we report the center (RA and Dec) used to build surface brightness profiles, the azimuthal and radial positions of the cold front and the mean value of $\Delta\alpha$.

Some clusters (e.g. Centaurus, A496, Perseus, A262) host more than one cold front. This phenomenon is not rare in cool core clusters. *Chandra* found multiple cold fronts in several systems such as A2204, A2029, Ophiuchus (Sanders et al. 2005; Clarke et al. 2004; Ascasibar & Markevitch 2006; Markevitch & Vikhlinin 2007). The existence of multiple cold fronts in such clusters is likely related to the origin and development of this phenomenon in cool cores (Ascasibar & Markevitch 2006; Markevitch & Vikhlinin 2007). We do not detect any cold front in some objects (i.e. A2204, A2029), which are well-known cold front systems (Sanders et al. 2005; Clarke et al. 2004). For these clusters, the cold front is located in very central regions ($14''$ and $30''$ from the center for A2029 and A2204, respectively). Therefore the discontinuity is well-resolved by *Chandra*, but it is hard to detect with *XMM-Newton*.

A last comment concerns the bias in the measure of the occurrence of cold fronts, which is caused by instrumental and observational limits: projection effects induce a smoothing on the surface brightness and temperature profiles and can hide a non-negligible fraction of cold fronts. Projection also completely hides cold fronts having an inclination greater than about 30° with respect to the plane of the sky. In addition, resolution limitations prevent the detection of cold fronts lying in the very central regions or cold fronts in distant clusters. Moreover, our detection algorithm may fail to detect some cold fronts with angular extension $< 30^\circ$. All these effects significantly reduce the ability to detect cold fronts. The frequency we find in our sample is therefore a lower limit of the true occurrence.

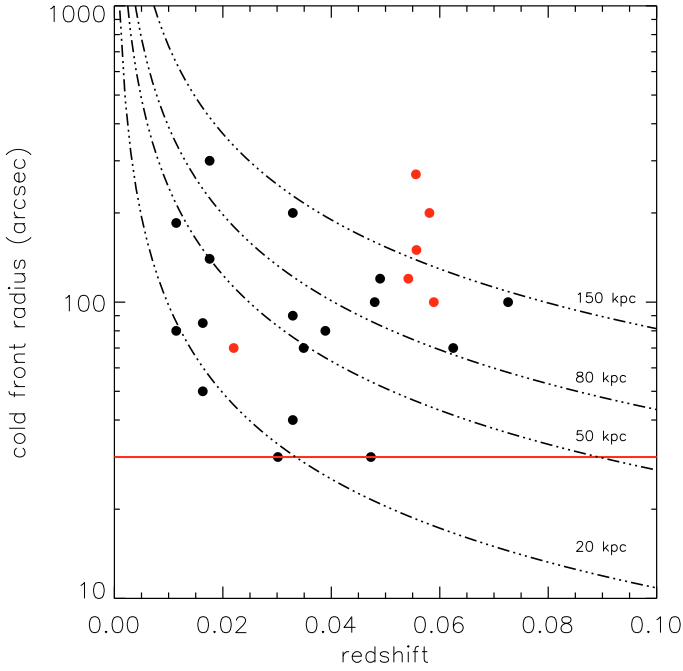


Fig. 4. Distances from the cluster center of the cold fronts detected in the sample plotted as a function of the redshift of their hosting systems. Red points label merging clusters (see Table 3) and black points label the remaining systems. We omitted in this figure A85* since the cold front lies in a subclump. Dot dashed lines plot fixed physical distances at the various redshifts. Red solid line marks the *XMM-Newton* resolution limit at $30''$.

5.2. Cold fronts occurrence: relation with redshift

In our sample, no cold fronts are detected in systems at redshifts greater than about 0.075. We have already remarked that A2204 and A2029 have been classified as cold front clusters from *Chandra* data analysis but we fail to detect their discontinuities because they lie at short distances ($\lesssim 30''$) from the X-ray peak, below the *XMM-Newton* resolution. For both A2204 and A2029, $z > 0.075$. This suggests that the lack of detection of cold fronts at the highest redshifts of the sample is most likely related to a resolution limit rather than to a real evolution. This effect is clearly shown in Fig. 4 where we plot the distances (in arcsec) from the cluster center of all the cold fronts detected in our sample as a function of the redshift of the systems they belong to. Red points label merging clusters (see Table 3 and Sect. 5.3.1) and black points label the remaining systems. Dashed dotted lines plot fixed physical distances (20, 50, 80, 150 kpc) at the various redshifts. From this figure, it is evident that cold fronts lying at ~ 20 – 80 kpc from the cluster center are only observed in nearby systems ($z \lesssim 0.05$). Moving towards higher redshifts where these physical distances progressively fall below the resolution limit ($30''$, red solid line in the figure) cold fronts cannot be detected anymore. For $z > 0.05$, we have only found cold fronts at distances $\gtrsim 80$ – 100 kpc from the cluster center, with a prominent presence of merging systems whose cold fronts are generally located at large distances from the core (see Sect. 5.3.1).

On the basis of the analysis of Fig. 4, we decided to apply a further selection on our sample by cutting the maximum redshift at $z = 0.075$ (i.e. the redshift where we stop detecting cold fronts). The resulting sample is reduced to 32 objects with a cold front occurrence of 59%. The sample may be biased against clusters having cold fronts at short distances from

the center, inducing an underestimation of the cold front occurrence we measure. However, in the case of cold fronts lying at distances $r \gtrsim 40$ kpc the sample can be considered, to a first approximation unaffected by a redshift bias.

5.3. Occurrence and origin of cold fronts

In this section, we investigate what distinguishes clusters without cold fronts from clusters hosting one or more.

5.3.1. Merger cold fronts

We start by focussing our attention on merger cold fronts. Some of our systems are well-known merging clusters. The morphology of these systems is generally complex, and no unique center can be identified in their surface brightness maps. In many of these systems (e.g. A3667 Vikhlinin et al. 2001a,b; Vikhlinin & Markevitch 2002; Briel et al. 2004), the merger process is occurring close to the plane of the sky, and the geometry of the event is clear. The origin and the evolution of cold fronts in these systems is most likely related to the merger process. More specifically, the motion of a cold dense core of a subsystem that moves in the atmosphere of the main cluster during a merger event induces the formation of a cold front feature. Typically, the subcluster is stripped of its outermost gas, and the ram pressure exerted on the surviving dense cloud by the less dense surrounding gas produces the contact discontinuity between the two subsystems, generating the cold front (Markevitch & Vikhlinin 2007).

In other objects, such as A3562 and A576, where the X-ray merger geometry is not as clear, the nature of the cold fronts we observe is not as obvious. A3562 is a cluster lying in the core of the Shapley supercluster, one of the highest mass concentrations in the local Universe. The presence of a radio halo in this cluster (Giacintucci et al. 2005) indicates a merger activity, since radio halos have only been found in interacting systems. Evidence of interaction also comes from *Beppo-SAX* data (Bardelli et al. 2002). Using *XMM-Newton* data, Finoguenov et al. (2004) suggest that the SC 1329–313 group southwest of A3562 has passed to the north of A3562, and the cluster core is likely oscillating in response to the passage of the group. A576 is another peculiar system whose discontinuity has also been observed with *Chandra* by Kempner & David (2004) who propose that the core of the cluster is the remnant of a merging subcluster. This picture was also suggested by Mohr et al. (1996) from an analysis of the galaxy population. Dupke et al. (2007) find that the system is consistent with a line-of-sight merger. According to this picture, the cold front we find in A576 is probably a merger cold front.

The clusters of our sample that host merger cold fronts are listed in the last part of Table 3 and marked with a bold-faced font. We include in this class A85*, the A85 subclump falling on the main structure. A576 and A3562, which are merging clusters where the cold front origin is not as readily associated to the merger event, are placed in a separate category and marked with an italic font in Table 3.

5.4. Non merger cold fronts: the entropy profile

In this section we investigate what distinguishes clusters without cold fronts from clusters hosting at least one, once we exclude the clusters having a merger cold front (see above Sect. 5.3.1) and clusters where the X-ray merger geometry is not clear. We focus on the remaining subsample (23 clusters) which includes both clusters undergoing a merger event that is not lying in the

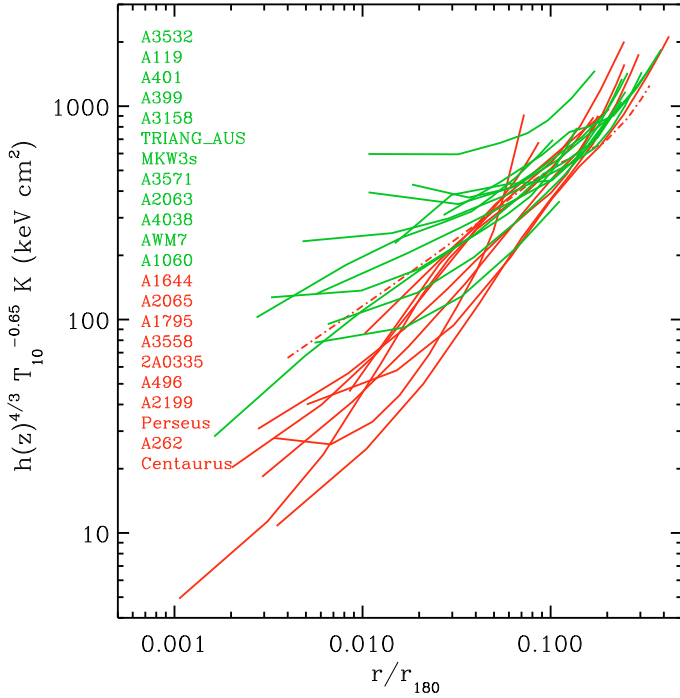


Fig. 5. Scaled entropy profiles for the subsample described in Sect. 5.4. Each curve is a locally weighted fit to the data points (see text for details) to reduce the scatter. Red solid lines are the profiles of clusters hosting cold fronts, while green solid lines are the profiles of clusters without cold fronts. The red dot dashed curve is the profile for A3558. Cygnus A is omitted (see text for details).

plane of the sky and clusters that do not present any sign of merging processes. In this subsample only 10 out of the 23 clusters host a cold front (main properties listed in the first part of Table 3). We try to understand what determines the existence of cold fronts in these systems, studying the radial entropy profile for each of these clusters. As is conventional in X-ray astronomy, we quantify the entropy using the adiabatic constant $K = kTn_e^{-2/3}$ (T and n_e are the gas temperature and density, respectively, and k is a constant) following Voit et al. (2005).

The specific entropy s is related to K through the relation $s \propto \ln K$. We refer to K as “entropy” throughout the paper. To obtain the entropy profiles, we derived the radial profiles of electron density n_e and temperature T , by deprojecting the observed surface brightness and temperature, under the assumption of spherical symmetry. The projected temperature and the surface brightness were derived through a spectral analysis of the clusters using concentric annuli (see Rossetti & Molendi 2010, for details). To perform deprojection, we adopted the procedure described in Ghizzardi et al. (2004).

In Fig. 5, we plot all the derived entropy profiles. Radii are scaled to r_{180} , the radius within which the mean density is 180 times the critical density¹. The values of r_{180} are derived using its relationship with the cluster mean temperature as in Arnaud et al. (2005) (see also Leccardi & Molendi 2008). The entropy is scaled using the empirical entropy scaling law $K \propto h(z)^{-4/3} T_{10}^{0.65}$, $h^2(z) = \Omega_m(1+z)^3 + \Omega_\Lambda$ (Pratt et al. 2006; Ponman et al. 2003), and T_{10} is the mean temperature of each cluster in units of 10 keV, as in Pratt et al. (2006). The curves plotted in Fig. 5 are actually a locally weighted regression (LOWESS

¹ $M_{180} = 180\rho_c(z)(4\pi/3)r_{180}^3$, where $\rho_c(z) = h^2(z)3H_0^2/8\pi G$ and $h^2(z) = \Omega_m(1+z)^3 + \Omega_\Lambda$.

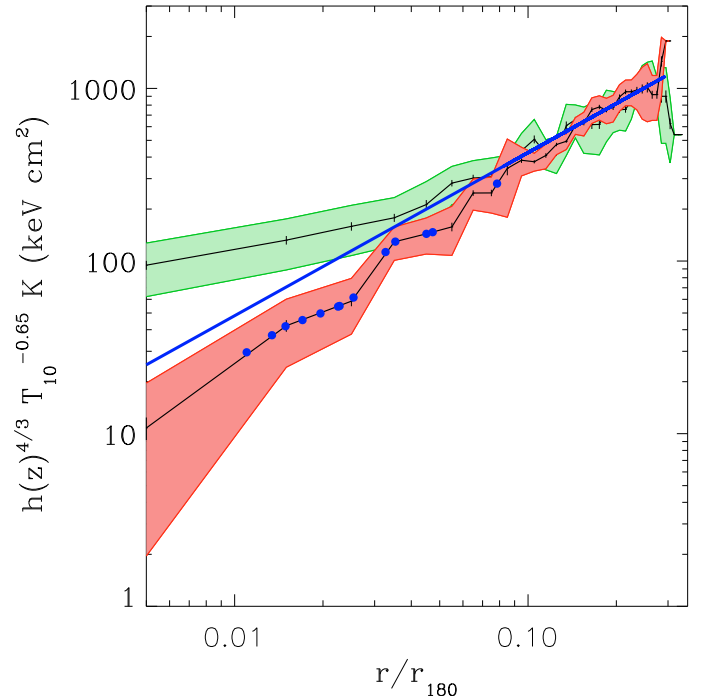


Fig. 6. Thin lines are the mean scaled entropy profiles for clusters hosting cold fronts (red area) and clusters without cold fronts (green area). The shaded areas represent the standard deviation from the mean profiles. The thick blue line is the power law obtained fitting all the profiles in the radial range $[0.08–0.3]r_{180}$. Blue points are the distances of the detected cold fronts (excluding A3558) from the cluster center.

regression, see Sanderson et al. 2006, 2005) in the log-log space to reduce the scatter and provide a better view of the profiles behavior. Clusters hosting a cold front (hereafter CF clusters) are shown along with clusters without cold fronts (hereafter NCF). We marked as particular case A3558. The behavior of this cluster will be discussed in Sect. 6.

The cluster Cygnus A has been discarded here because of the strong contamination by the central AGN: the presence of the two hot spots invalidates the assumption of spherical symmetry and does not allow to deproject the temperature and surface brightness radial profiles. Figure 5 shows that all the profiles follow a similar trend at large radii ($r \gtrsim 0.08r_{180}$). Moving towards the innermost regions, the profiles spread out so we observe a large scatter. More precisely, the NCF clusters typically have central entropies higher than CF clusters. Moreover, systems hosting cold fronts seem to have a steeper profile than clusters without cold fronts.

In Fig. 6 we plot the two averaged profiles for CF and NCF clusters. The shaded areas represent the standard deviation from the mean profiles. As in Fig. 5, color codes label CF clusters (red area) and NCF clusters (green area). We find that the mean profiles are similar at large radii. Fitting all the entropy profiles with a power law in the radial range $[0.08–0.3]r_{180}$, we find a slope $\alpha = 0.95 \pm 0.01$. For comparison, Pratt et al. (2006) find a slope $\alpha = 1.14 \pm 0.06$, while, Pratt & Arnaud (2005) find $\alpha = 0.94 \pm 0.14$, and Piffaretti et al. (2005) find $\alpha = 0.95 \pm 0.02$. Restricting to $[0.1–0.3]r_{180}$ we find a slightly steeper power law with $\alpha = 1.08 \pm 0.02$ in accordance with the theoretical value of 1.1 predicted by Tozzi & Norman (2001) (see also Voit & Ponman 2003; Borgani et al. 2002).

Moving towards the innermost regions, for $r \lesssim 0.08r_{180}$, the two mean profiles decouple. The NCF mean cluster profile

exhibits a central entropy excess with respect to the outer power law model. The slope in the $[0.01-0.08]r_{180}$ range is $\alpha = 0.64 \pm 0.01$ significantly lower than the outer power law slope. In contrast, the CF cluster profiles become steeper in the same radial range, reaching lower central values. By fitting the CF mean entropy profile with a power law in the $[0.01-0.08]r_{180}$ range, we find a slope of 1.22 ± 0.01 , significantly higher than the external power law slope. The mean entropy values in the innermost bin ($r = 0.005r_{180}$) are $94.5 \pm 5.5 \text{ keV cm}^2$ and $10.8 \pm 1.6 \text{ keV cm}^2$ for NCF and CF clusters, respectively. Excluding the particular case A3558 (see Sect. 6) does not significantly change results on best-fit values.

Since the steepness of the entropy profile is an indicator of the presence of a “cool core” (e.g. Cavagnolo et al. 2009), clusters with a steep entropy profile are also likely to feature a temperature decrement and a brightness excess in their internal regions. Therefore, one may argue that we do not detect cold fronts in objects with a flat entropy profile just because their surface brightness is lower than that of clusters where we do detect cold fronts. However, as can be seen from the profiles reported in the Appendix, we detect cold fronts in the centers of cool core objects (e.g. A262) where the SB is high, but also in the outer regions of merging clusters where the SB is much lower (e.g., A3667, A85*). In Fig. 3, we show an example of a cluster where we do not detect CF, AWM7, which has an SB comparable to those of the clusters where we do detect cold fronts. This is the case for almost all the clusters of our remaining sample where we do not detect cold fronts.

6. Discussion

The origin of cold fronts in clusters manifestly undergoing a merger event can be related to the motion of a dense cold cloud of gas within the atmosphere of another subcluster. Conversely, the presence (or the absence) of these features in the subsample of non merging clusters and clusters where the merger is not close to the plane of the sky is not clearly understood. Figure 6 provides some hints to help understand what determines the presence of cold fronts in these systems. The general picture emerging here is that the entropy profile discriminates among the two classes (CF and NCF) of clusters. While at large radii the (scaled) entropy profiles of these clusters are very similar, their behaviors differ in the innermost regions ($r \lesssim 0.08r_{180}$).

Our finding of a steep entropy gradient in CF cluster agrees with theoretical expectations. Indeed, simulations by Ascasibar & Markevitch (2006) show that cold fronts can rise and develop in the cores of clusters if the entropy sharply decreases towards the center (as typically occurs in the center of cool core clusters). According to these simulations, cold fronts develop as a consequence of minor merger events; during its passage near the center of a cluster, a merging subclump induces some disturbance on the low entropy gas of the core and displaces it from the center of the potential well. If the entropy profile is steep, the cool gas starts sinking towards the minimum of the gravitational potential, a sloshing mechanism sets in, and cold fronts arise. If the entropy profile is not steep, the entropy contrast is insufficient for the cool gas to flow back and for the sloshing mechanism to set in. In agreement with this picture, we find that cold fronts only form in regions where the entropy profile sharply decreases. In Fig. 6, we plot the cold front positions measured for the non merging clusters of our sample. Excluding the outermost cold front of A496 (this cluster hosts three cold fronts) which lies at a distance of $\sim 0.08r_{180}$ from the peak, all the cold fronts we detect lie at distances smaller than $\sim 0.05r_{180}$, where entropy

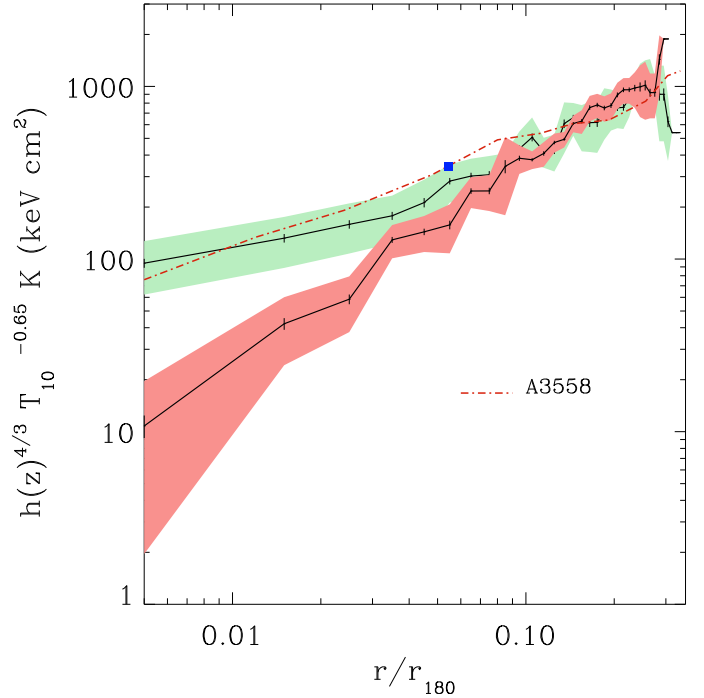


Fig. 7. Mean scaled entropy profiles as in Fig. 6. Red dot-dashed curve is the profile of A3558. The blue filled square is the A3558 cold front distance from the cluster center.

profiles steepen, and greater than $\sim 0.01r_{180}$ where, in many systems, *Chandra* detects a flattening (Donahue et al. 2006).

The large majority of clusters of the final subsample obey the general rule that cold fronts are hosted by systems with a steep entropy profile in their centers. However, as already pointed out, A3558 is a peculiar case because although its entropy profile is similar to the NCF clusters profiles, it hosts a cold front. Some comments are needed to understand why this outlier does not follow the general behavior. The cold front for A3558 (Fig. 7) is located at greater distance ($r \sim 0.05r_{180}$) than all the other cold fronts we detect, in a region where a weak entropy gradient is present, but not as sharp as in the other CF clusters profiles.

This cluster lies at the center of the Shapley supercluster, and its special behavior is likely related to the unique environment in which it is embedded. To understand the reason cold fronts can arise in such a system, we refer once more to Ascasibar & Markevitch (2006) simulations. When the entropy profile of the cluster does not sharply decrease in the center, the central cold gas is easily pushed away from the dark matter peak, at the merging subclump passage. Accordingly, the cold front emerges far from the core. However, there is no entropy contrast to trigger the sloshing mechanism, and this cold front will not develop further. Cold fronts rising in these systems are short-lived, hence rare phenomena (see Fig. 12 in Ascasibar & Markevitch 2006). A3558 is embedded in a very unrelaxed environment where merging events are frequent, making the probability to form (and to observe) such fronts higher. Alternatively, this cold front might be a merger cold front that we failed to recognize because A3558 cannot be classified easily as a merging cluster. As discussed in Rossetti et al. (2007), it presents some features similar to those of cool core clusters and other properties that are more common in merging clusters.

One of the main findings of our paper is that we detect at least one cold front in all steep entropy gradient clusters in the final subsample. Ascasibar & Markevitch (2006) show that, once

the sloshing mechanism sets in, cold fronts can be recognized in all the projection planes, even if they are more prominent on the merger plane (see Fig. 19 of their paper). However, the limited resolution of our instruments allow us to recognize only the most apparent brightness discontinuity. Indeed, we performed some simulations of cold front projection with the *XMM-Newton* PSF and found that cold fronts can only be observed if they lie within some 30° of the plane of the sky. This means that our 100% detection rate implies that most steep entropy clusters must host more than one “prominent” cold front. This abundance of cold fronts suggests that, whatever the triggering mechanism might be, it must have a high occurrence rate. Since the prominent cold fronts that we can detect are located on the merger plane, the detection of one or more cold fronts in all our steep entropy systems seems to indicate that a sizeable fraction of them are currently experiencing more than one minor merger. Assuming that, crudely speaking, cold fronts are visible on a timescale of about 3 Gyr (this is the case for the dark matter + gas simulation in [Ascasibar & Markevitch 2006](#), while for the dark matter only simulations, this timescale is longer), our cold front detection rate translates into a minimum merger frequency of 1/3 merger event per halo per Gyr. If we further assume a minimum mass ratio of 1/10, we can compare our rate with rates expected from cosmological simulations. Using Fig. 8 in a recent paper by [Fakhouri & Ma \(2008\)](#) we find a merger rate of ~ 0.2 merger per halo per Gyr for a mass ratio higher than 1/10. This is somewhat smaller than the minimum rate implied by our observed cold front rates; however, given the numerous simplifications we applied in our calculation, we deem it to be in acceptable agreement.

Gas sloshing may provide an important contribution to the cooling-heating problem in cool core clusters ([ZuHone et al. 2009](#)). The sloshing gas typically moves at sub-(or trans-)sonic velocities carrying a kinetic energy comparable to the thermal energy, but the dissipation of this kinetic energy to thermal energy is too slow compared to cooling ([Markevitch et al. 2001](#)). However, the sloshing mechanism also brings the outer high entropy gas into the core, mixing it with the cooling gas and resulting in a heat inflow which can prevent the formation of a “cooling flow” for periods of time 1–3 Gyr ([ZuHone et al. 2009](#)). If subcluster encounters are frequent enough, as suggested by our high detection rate, the sloshing mechanism can efficiently offset cooling. Intriguingly the sloshing mechanism operates preferentially in steep entropy profile clusters, i.e. precisely those which require heating to offset the cooling. With the coming into operation of the first space-borne micro-calorimeter, most likely the one onboard the ASTRO-H mission ([Takahashi et al. 2008](#)), it will be possible to investigate gas motions in the direction of the line of sight, i.e. orthogonally with respect to that of the plane of the sky sampled with cold fronts. The combination of these two pieces of informations will allow a reliable estimate of the motions of the ICM in clusters core and estimate their role in offsetting cooling.

7. Summary

We performed a systematic search of cold fronts using *XMM-Newton* data for a sample of 45 objects extracted from the B55 flux limited sample ([Edge et al. 1990](#)). The main results of our work are the following:

- Excluding three unclassified cases, we find that 19 clusters out of 42 host at least one cold front.

- We do not detect any cold front in systems having redshift greater than about 0.075. This is most likely related to *XMM-Newton* resolution limit. By cutting our sample at $z = 0.075$, we restrict our sample to 32 objects with a cold front occurrence of 59%.
- Cold fronts are easily detected in systems that are manifestly undergoing a merger event in (or close to) the plane of the sky.
- Out of the 23 clusters of the remaining subsample (systems undergoing a merger event that is not lying in the plane of the sky and non-merging clusters), 10 objects exhibit a cold front. For this final subsample, the entropy profile of systems hosting cold fronts is found to be steeper than that of clusters without them. The difference is observed at radii smaller than about $0.08 r_{180}$ where all our cold fronts are found.
- Our findings agree with simulation-based predictions. As shown by [Ascasibar & Markevitch \(2006\)](#), an entropy gradient is a necessary ingredient for triggering gas sloshing.
- Since projection effects strongly limit the capability of detecting cold fronts, the finding that all the clusters with a steep entropy profile host a cold front implies that most clusters with a steep entropy profile must have more than one cold front.
- Under the assumption that cold fronts in cool core clusters are triggered by minor mergers, we estimate a minimum of 1/3 events per halo per Gyr, which is somewhat higher than that expected from cosmological simulations ([Fakhouri & Ma 2008](#)).
- Gas sloshing may provide an important contribution to the cooling-heating problem in cool core clusters. A robust assessment of the gas motions associated to the sloshing phenomenon will become possible once the first space-borne microcalorimeter is operating.

Acknowledgements. The authors thank the referee for useful comments. The authors are pleased to acknowledge Sabrina De Grandi and Fabio Gastaldello, whose suggestions have significantly improved the paper.

References

- Arnaud, M., Pointecouteau, E., & Pratt, G. W. 2005, *A&A*, 441, 893
- Ascasibar, Y., & Markevitch, M. 2006, *ApJ*, 650, 102
- Baldi, A., Molendi, S., Comastri, A., et al. 2002, *ApJ*, 564, 190
- Bardelli, S., De Grandi, S., Ettori, S., et al. 2002, *A&A*, 382, 17
- Blanton, E. L., Douglass, E. M., Sarazin, C. L., Clarke, T. E., & McNamara, B. R. 2007, in *Heating versus Cooling in Galaxies and Clusters of Galaxies*, ed. H. Böhringer, G. W. Pratt, A. Finoguenov, & P. Schuecker, 109
- Blanton, E. L., Sarazin, C. L., McNamara, B. R., & Wise, M. W. 2001, *ApJ*, 558, L15
- Blanton, E. L., Sarazin, C. L., & McNamara, B. R. 2003, *ApJ*, 585, 227
- Borgani, S., Governato, F., Wadsley, J., et al. 2002, *MNRAS*, 336, 409
- Briel, U. G., Finoguenov, A., & Henry, J. P. 2004, *A&A*, 426, 1
- Cappellari, M., & Copin, Y. 2003, *MNRAS*, 342, 345
- Cavagnolo, K. W., Donahue, M., Voit, G. M., & Sun, M. 2009, *ApJS*, 182, 12
- Churazov, E., Forman, W., Jones, C., & Böhringer, H. 2003, *ApJ*, 590, 225
- Clarke, T. E., Blanton, E. L., & Sarazin, C. L. 2004, *ApJ*, 616, 178
- Diehl, S., & Statler, T. S. 2006, *MNRAS*, 368, 497
- Donahue, M., Horner, D. J., Cavagnolo, K. W., & Voit, G. M. 2006, *ApJ*, 643, 730
- Dupke, R., & White, III, R. E. 2003, *ApJ*, 583, L13
- Dupke, R. A., Mirabal, N., Bregman, J. N., & Evrard, A. E. 2007, *ApJ*, 668, 781
- Durret, F., Forman, W., Gerbal, D., Jones, C., & Vikhlinin, A. 1998, *A&A*, 335, 41
- Edge, A. C., Stewart, G. C., Fabian, A. C., & Arnaud, K. A. 1990, *MNRAS*, 245, 559
- Fabian, A. C., Sanders, J. S., Allen, S. W., et al. 2003, *MNRAS*, 344, L43
- Fabian, A. C., Sanders, J. S., Taylor, G. B., et al. 2006, *MNRAS*, 366, 417
- Fakhouri, O., & Ma, C.-P. 2008, *MNRAS*, 386, 577
- Finoguenov, A., Henriksen, M. J., Briel, U. G., de Plaa, J., & Kaastra, J. S. 2004, *ApJ*, 611, 811

- Forman, W., Jones, C., Churazov, E., et al. 2007, *ApJ*, 665, 1057
- Ghizzardi, S., Molendi, S., Pizzolato, F., & De Grandi, S. 2004, *ApJ*, 609, 638
- Giacintucci, S., Venturi, T., Brunetti, G., et al. 2005, *A&A*, 440, 867
- Heinz, S., Churazov, E., Forman, W., Jones, C., & Briel, U. G. 2003, *MNRAS*, 346, 13
- Kempner, J. C., & David, L. P. 2004, in *The Riddle of Cooling Flows in Galaxies and Clusters of galaxies*, ed. T. Reiprich, J. Kempner, & N. Soker, 57
- Kempner, J. C., Sarazin, C. L., & Ricker, P. M. 2002, *ApJ*, 579, 236
- Lane, W. M., Clarke, T. E., Taylor, G. B., Perley, R. A., & Kassim, N. E. 2004, *AJ*, 127, 48
- Leccardi, A., & Molendi, S. 2008, *A&A*, 486, 359
- Markevitch, M., & Vikhlinin, A. 2007, *Phys. Rep.*, 443, 1
- Markevitch, M., Gonzalez, A. H., David, L., et al. 2002, *ApJ*, 567, L27
- Markevitch, M., Ponman, T. J., Nulsen, P. E. J., et al. 2000, *ApJ*, 541, 542
- Markevitch, M., Vikhlinin, A., & Forman, W. R. 2003, in *Astronomical Society of the Pacific Conference Series*, ed. S. Bowyer, & C.-Y. Hwang, ASP Conf. Ser., 301, 37
- Markevitch, M., Vikhlinin, A., & Mazzotta, P. 2001, *ApJ*, 562, L153
- Marty, P. B., Kneib, J.-P., Sadat, R., Ebeling, H., & Smail, I. 2003, in *Presented at the Society of Photo-Optical Instrumentation Engineers (SPIE) Conference*, ed. J. E. Truemper & H. D. Tananbaum, Conf. Ser. 4851, 222
- Mathis, H., Lavaux, G., Diego, J. M., & Silk, J. 2005, *MNRAS*, 357, 801
- Mazzotta, P., Edge, A. C., & Markevitch, M. 2003, *ApJ*, 596, 190
- Mazzotta, P., Markevitch, M., Vikhlinin, A., et al. 2001, *ApJ*, 555, 205
- McNamara, B. R., & Nulsen, P. E. J. 2007, *ARA&A*, 45, 117
- McNamara, B. R., Nulsen, P. E. J., Wise, M. W., et al. 2005, *Nature*, 433, 45
- McNamara, B. R., Wise, M., Nulsen, P. E. J., et al. 2000, *ApJ*, 534, L135
- Mohr, J. J., Geller, M. J., Fabricant, D. G., et al. 1996, *ApJ*, 470, 724
- Nagai, D., & Kravtsov, A. V. 2003, *ApJ*, 587, 514
- Nulsen, P. E. J., David, L. P., McNamara, B. R., et al. 2002, *ApJ*, 568, 163
- Nulsen, P. E. J., McNamara, B. R., Wise, M. W., & David, L. P. 2005, *ApJ*, 628, 629
- Owers, M. S., Nulsen, P. E. J., Couch, W. J., & Markevitch, M. 2009, *ApJ*, 704, 1349
- Peres, C. B., Fabian, A. C., Edge, A. C., et al. 1998, *MNRAS*, 298, 416
- Piffaretti, R., Jetzer, P., Kaastra, J. S., & Tamura, T. 2005, *A&A*, 433, 101
- Ponman, T. J., Sanderson, A. J. R., & Finoguenov, A. 2003, *MNRAS*, 343, 331
- Pratt, G. W., & Arnaud, M. 2002, *A&A*, 394, 375
- Pratt, G. W., & Arnaud, M. 2005, *A&A*, 429, 791
- Pratt, G. W., Arnaud, M., & Pointecouteau, E. 2006, *A&A*, 446, 429
- Reiprich, T. H., & Böhringer, H. 2002, *ApJ*, 567, 716
- Roettiger, K., Loken, C., & Burns, J. O. 1997, *ApJS*, 109, 307
- Roettiger, K., Stone, J. M., & Mushotzky, R. F. 1998, *ApJ*, 493, 62
- Rossetti, M., Ghizzardi, S., Molendi, S., & Finoguenov, A. 2007, *A&A*, 463, 839
- Rossetti, M., & Molendi, S. 2010, *A&A*, 510, 83
- Sanders, J. S., Fabian, A. C., & Taylor, G. B. 2005, *MNRAS*, 356, 1022
- Sanderson, A. J. R., Finoguenov, A., & Mohr, J. J. 2005, *ApJ*, 630, 191
- Sanderson, A. J. R., Ponman, T. J., & O'Sullivan, E. 2006, *MNRAS*, 372, 1496
- Takahashi, T., Kelley, R., Mitsuda, K., et al. 2008, in *Society of Photo-Optical Instrumentation Engineers (SPIE) Conf. Ser.*, 7011
- Tittley, E. R., & Henriksen, M. 2005, *ApJ*, 618, 227
- Tozzi, P., & Norman, C. 2001, *ApJ*, 546, 63
- Vikhlinin, A., Markevitch, M., & Murray, S. S. 2001a, *ApJ*, 551, 160
- Vikhlinin, A., Markevitch, M., & Murray, S. S. 2001b, *ApJ*, 549, L47
- Vikhlinin, A. A., & Markevitch, M. L. 2002, *Astron. Lett.*, 28, 495
- Voit, G. M., & Ponman, T. J. 2003, *ApJ*, 594, L75
- Voit, G. M., Bryan, G. L., Balogh, M. L., & Bower, R. G. 2002, *ApJ*, 576, 601
- Voit, G. M., Kay, S. T., & Bryan, G. L. 2005, *MNRAS*, 364, 909
- Wise, M. W., McNamara, B. R., Nulsen, P. E. J., Houck, J. C., & David, L. P. 2007, *ApJ*, 659, 1153
- ZuHone, J. A., Markevitch, M., & Johnson, R. E. 2009, *ApJ*, accepted [arXiv:astro-ph:0912.0237]

Appendix A: Surface brightness and temperature profiles

In this Appendix we report the EPIC flux images of the clusters of the sample where we detected cold fronts (Figs. A.1–A.5). The figures show the flux images in the 0.4–2 keV band, the black arcs indicate the position of the cold fronts, and the “X” symbol the selected center for the extraction of the profiles. In Figs. A.6–A.11, we show the surface brightness and temperature profiles across the discontinuities in a representative sectors for all the cold fronts reported in Table 3. For each plot the discontinuity region is marked with vertical red dashed lines.

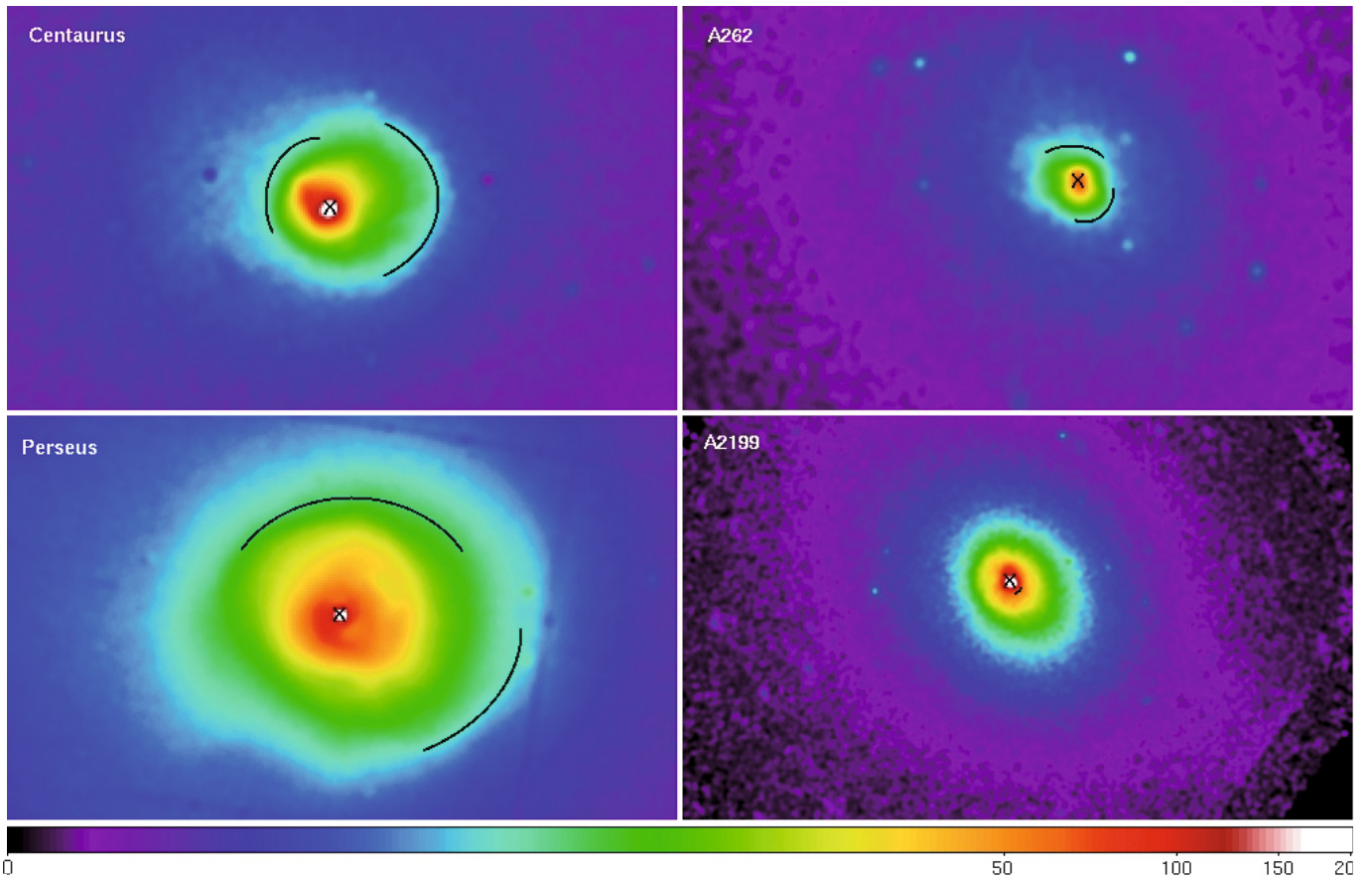


Fig. A.1. EPIC flux images for Centaurus, A262, Perseus, and A2199.

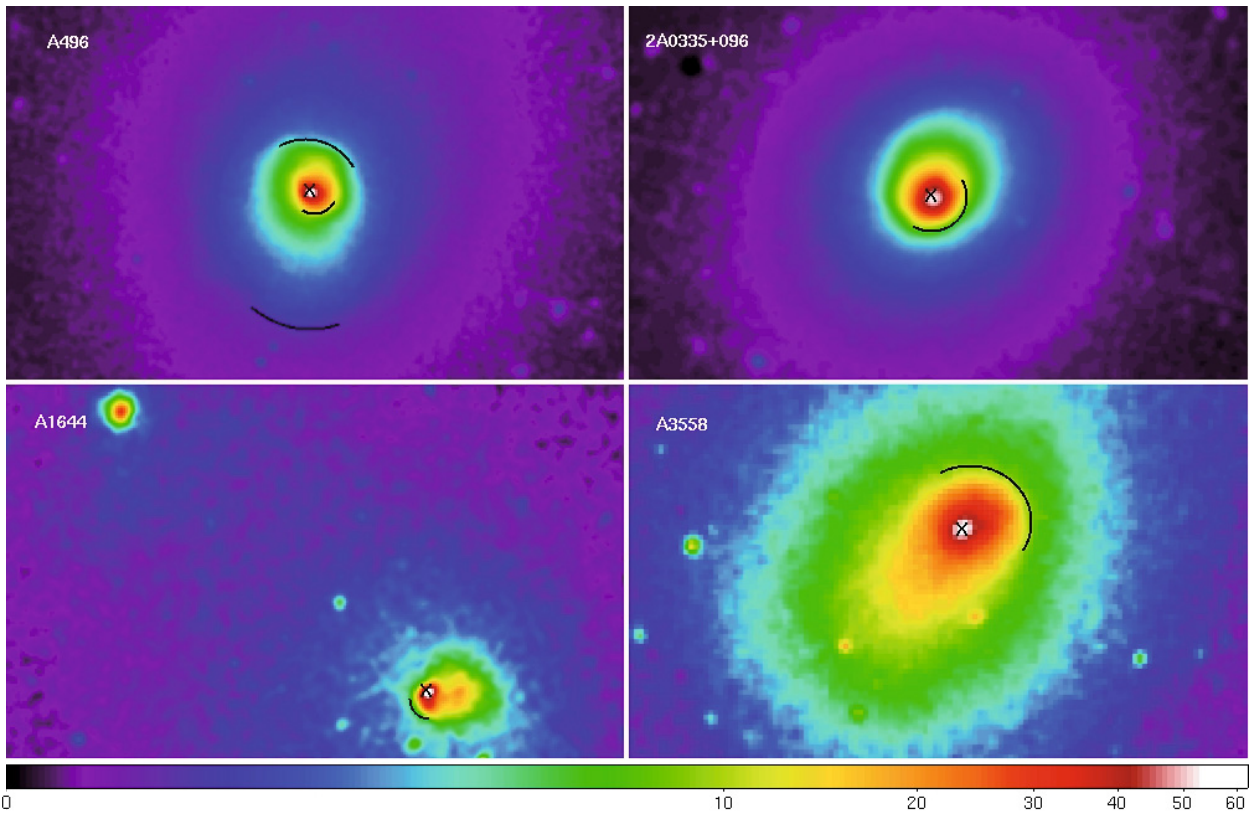


Fig. A.2. EPIC flux images for 2A0335, A3558, A496, and A1644.

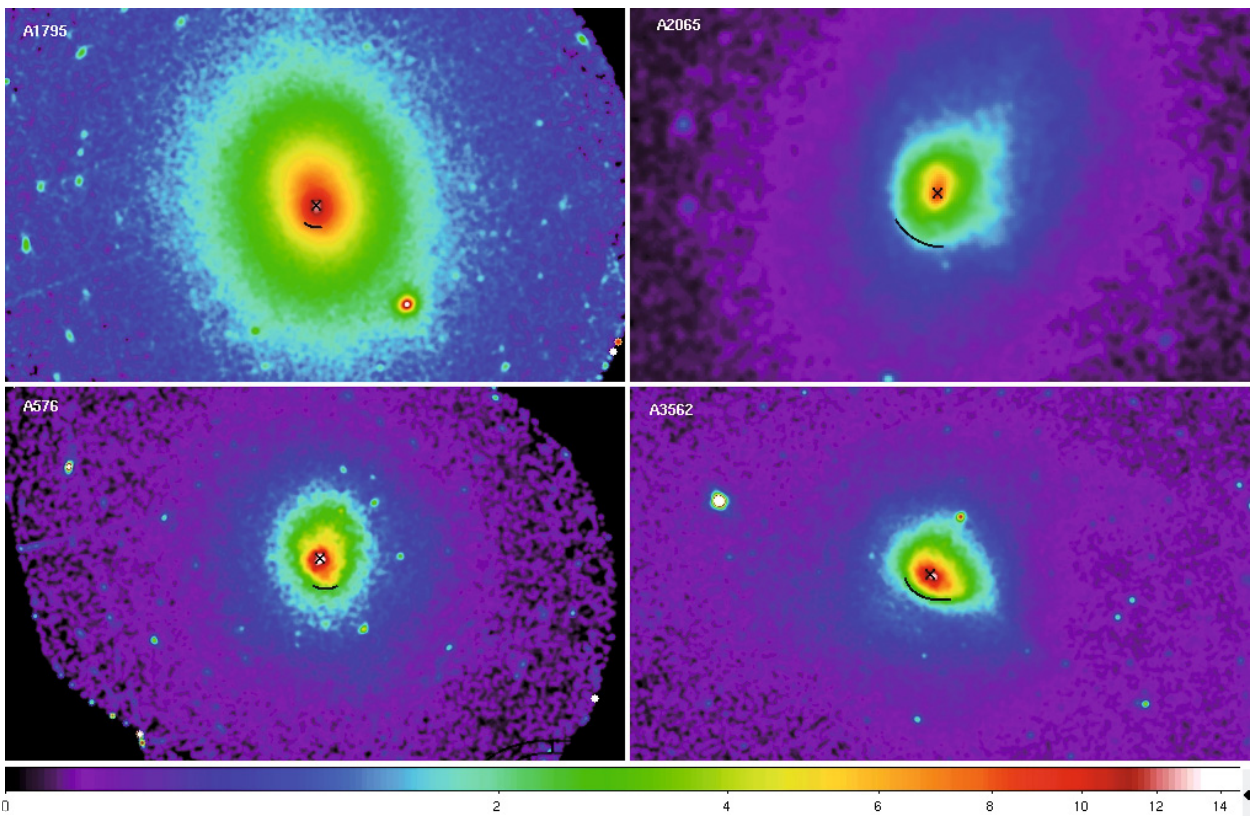


Fig. A.3. EPIC flux images for A2065, A3562, A1795, and A576.

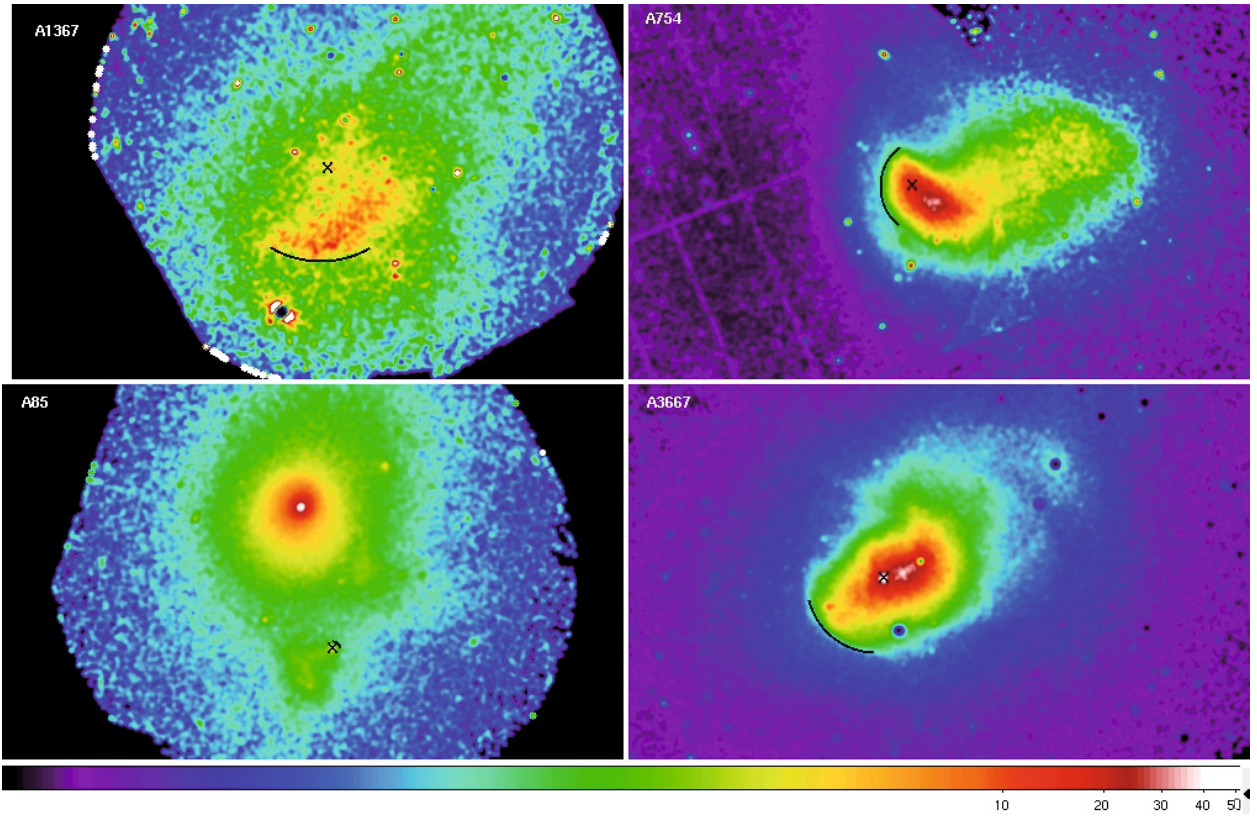


Fig. A.4. EPIC flux images for A754, A3667, A1367, and A85.

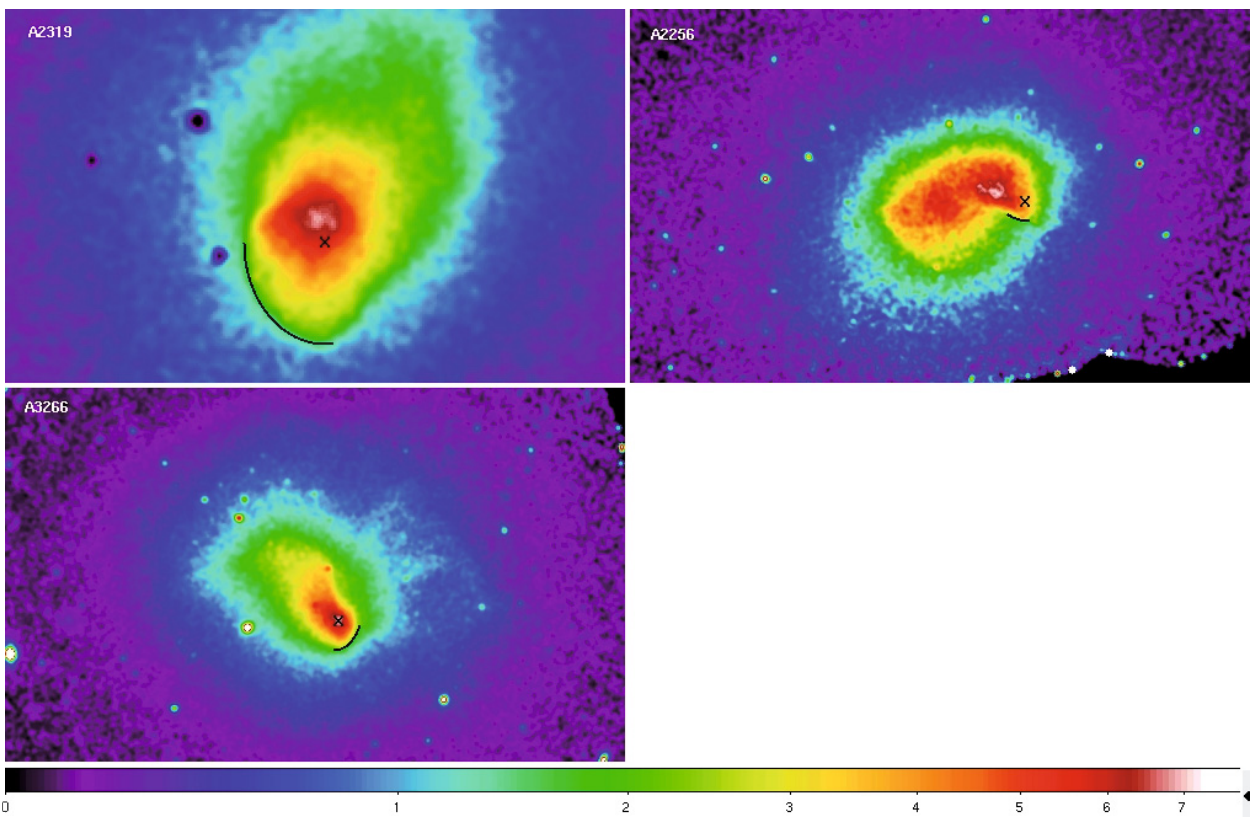


Fig. A.5. EPIC flux images for A2256, A2319, and A3266.

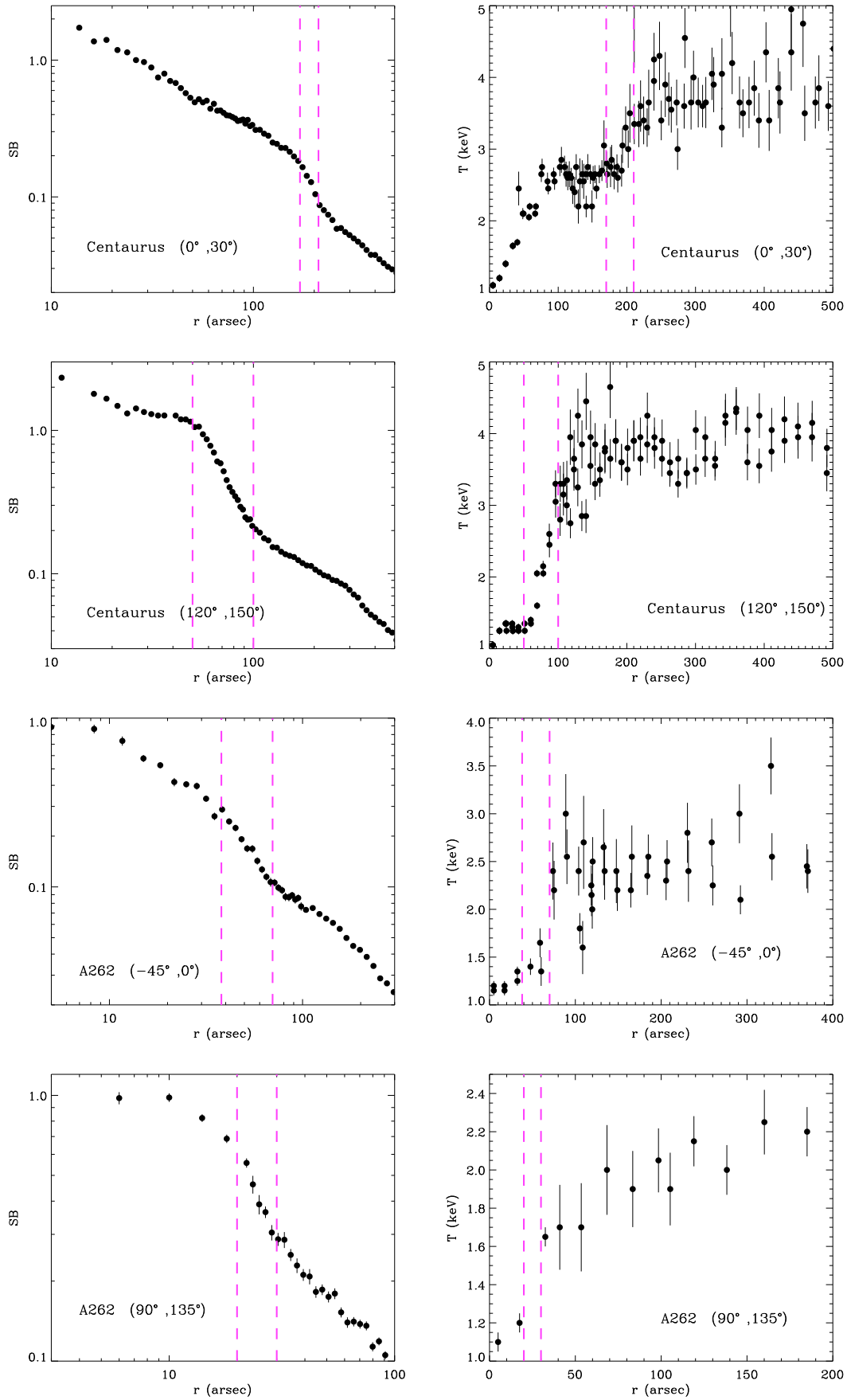


Fig. A.6. Surface brightness and temperature profiles for the cold fronts in Centaurus and A262.

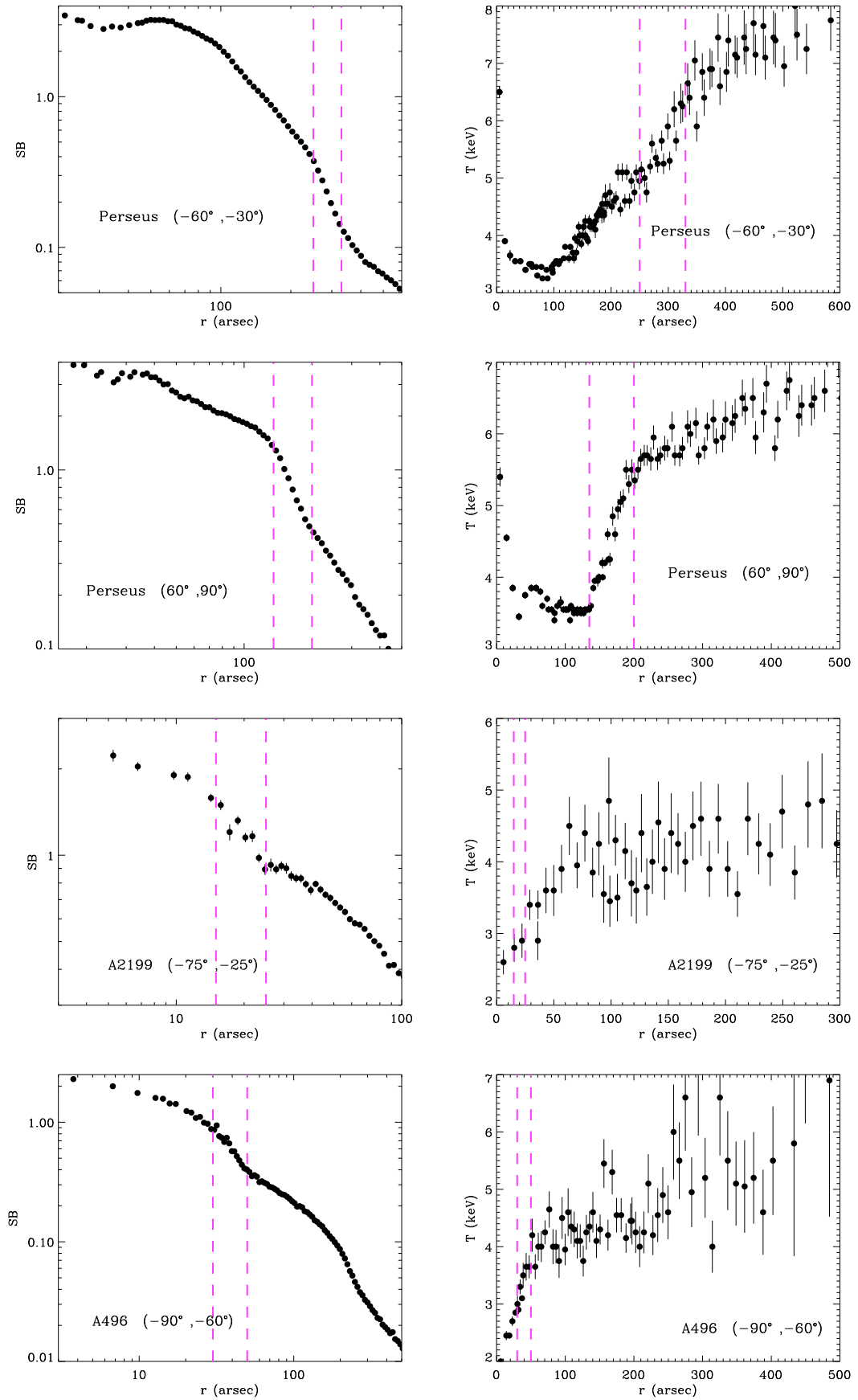


Fig. A.7. Surface brightness and temperature profiles for the cold fronts in Perseus, A2199, and A496.

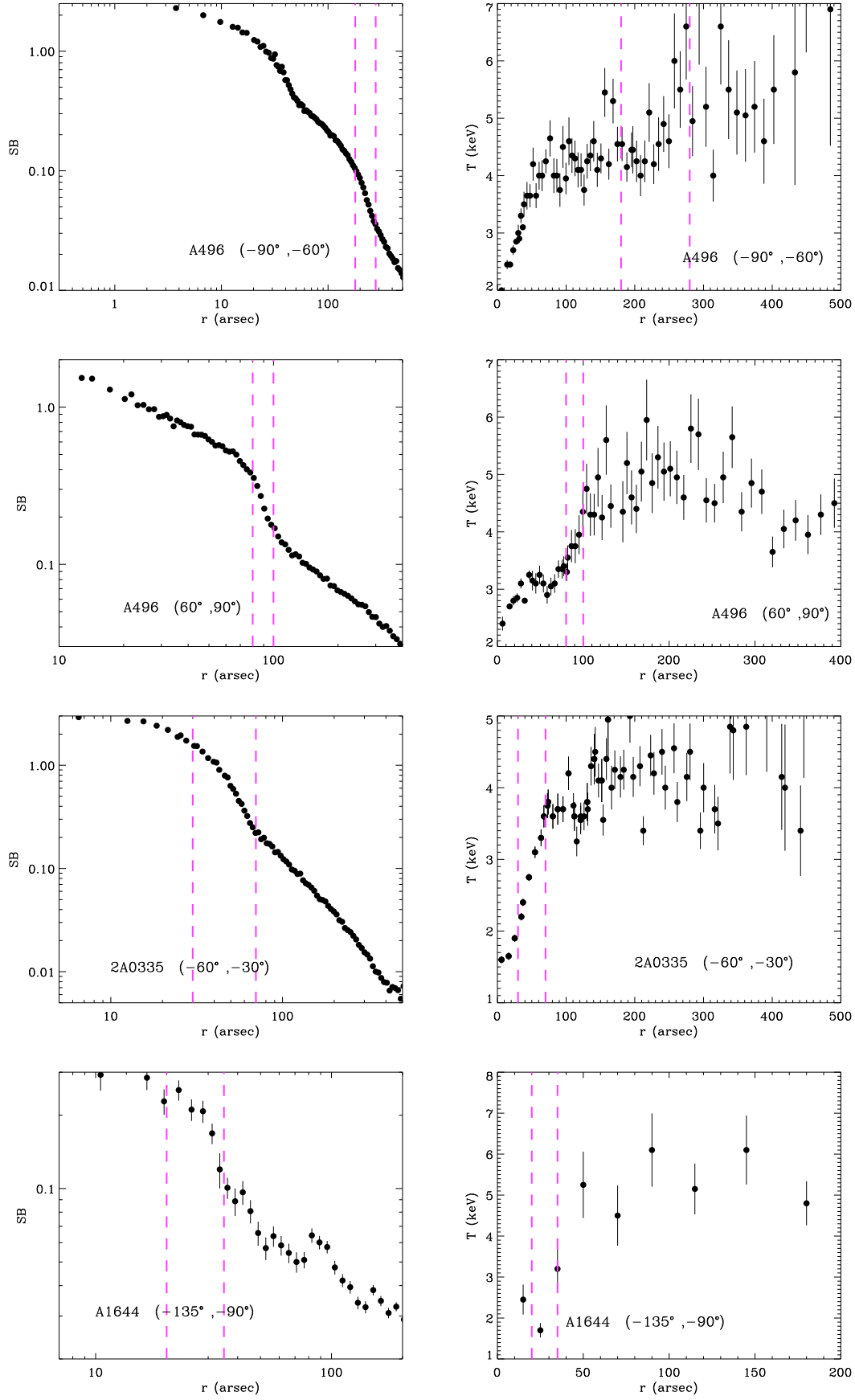


Fig. A.8. Surface brightness and temperature profiles for the cold fronts in A496, 2A0335, and A1644.

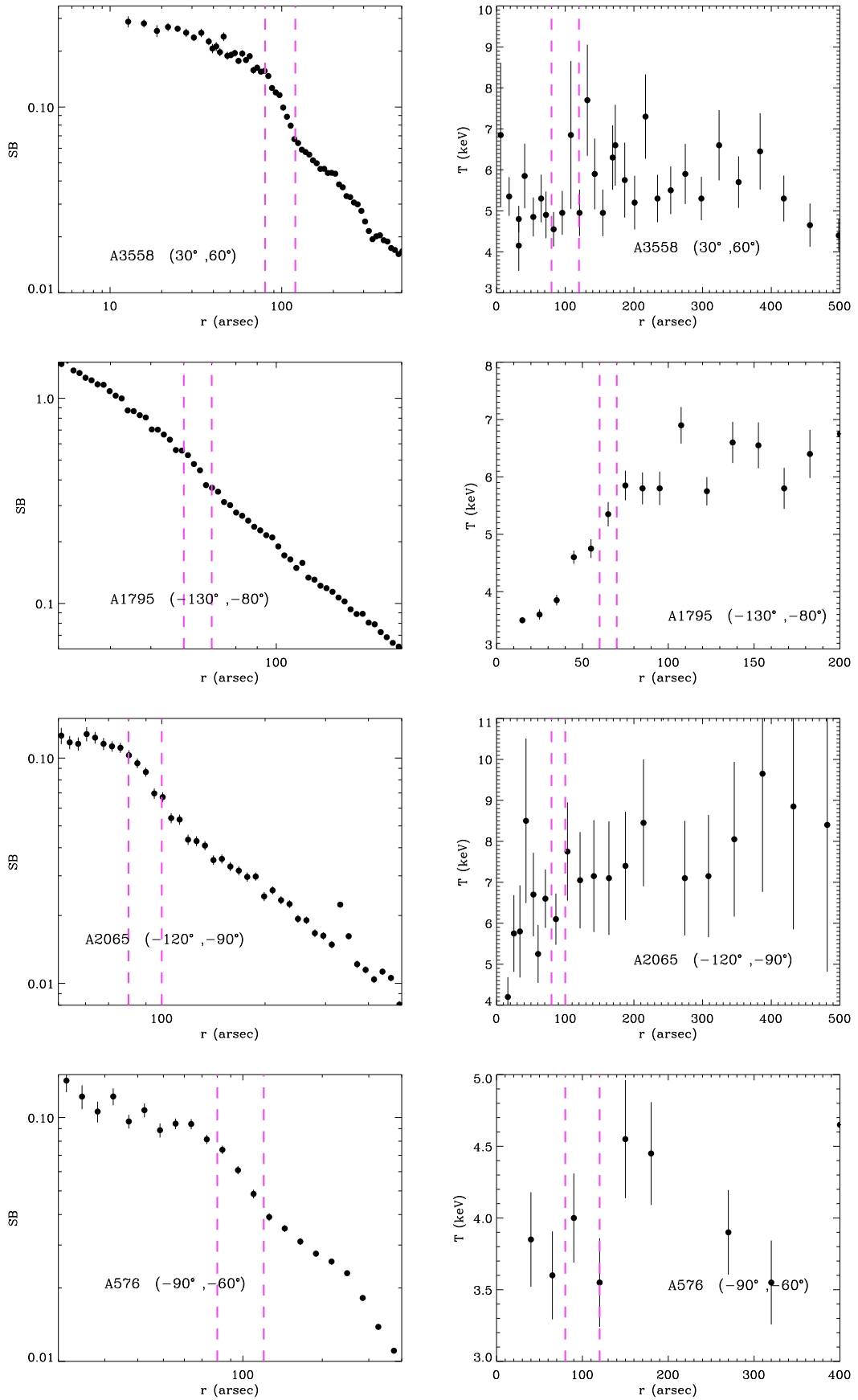


Fig. A.9. Surface brightness and temperature profiles for the cold fronts in A3558, A1795, A2065, and A576.

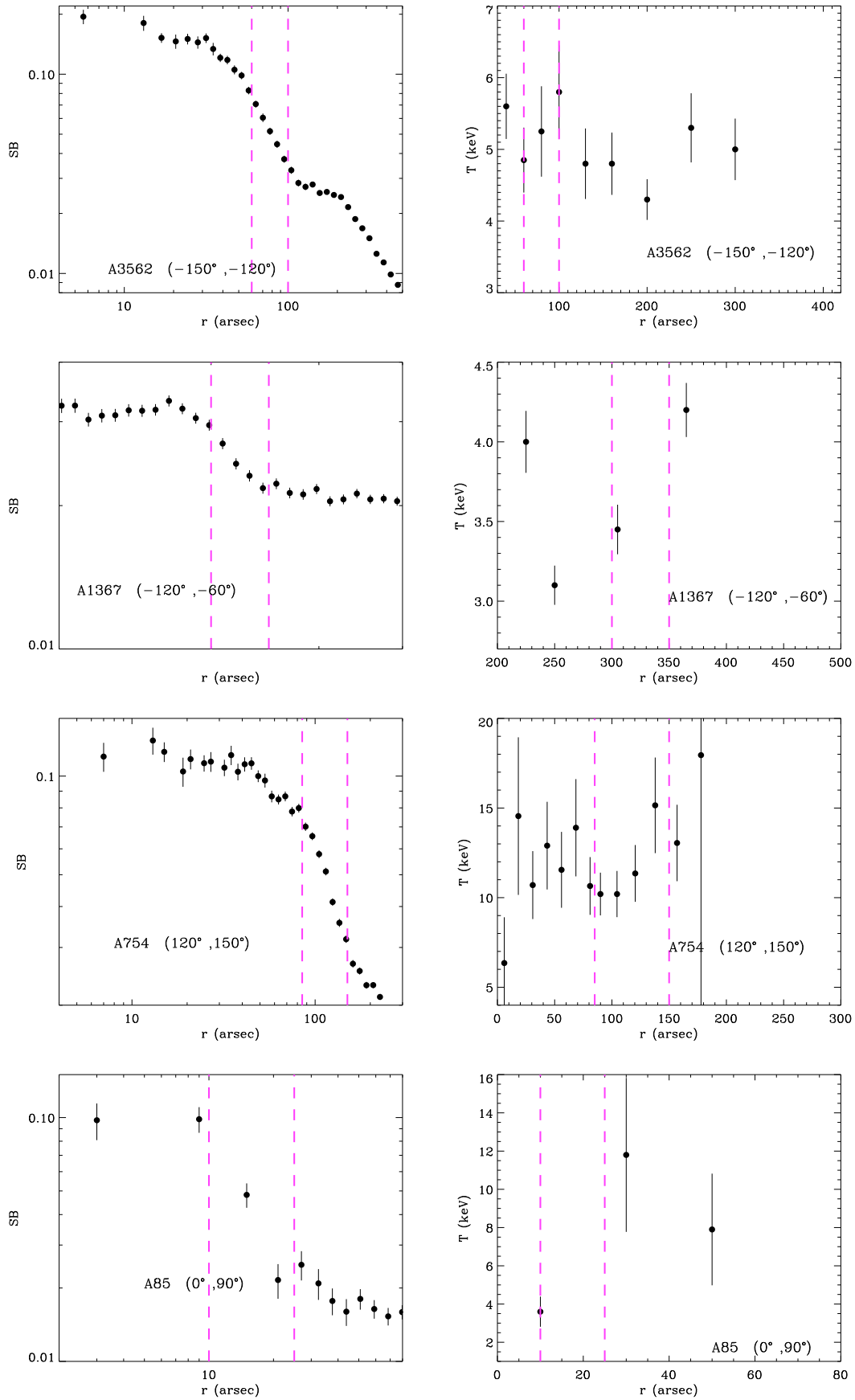


Fig. A.10. Surface brightness and temperature profiles for the cold fronts in A3562, A1367, A754, and A85*.

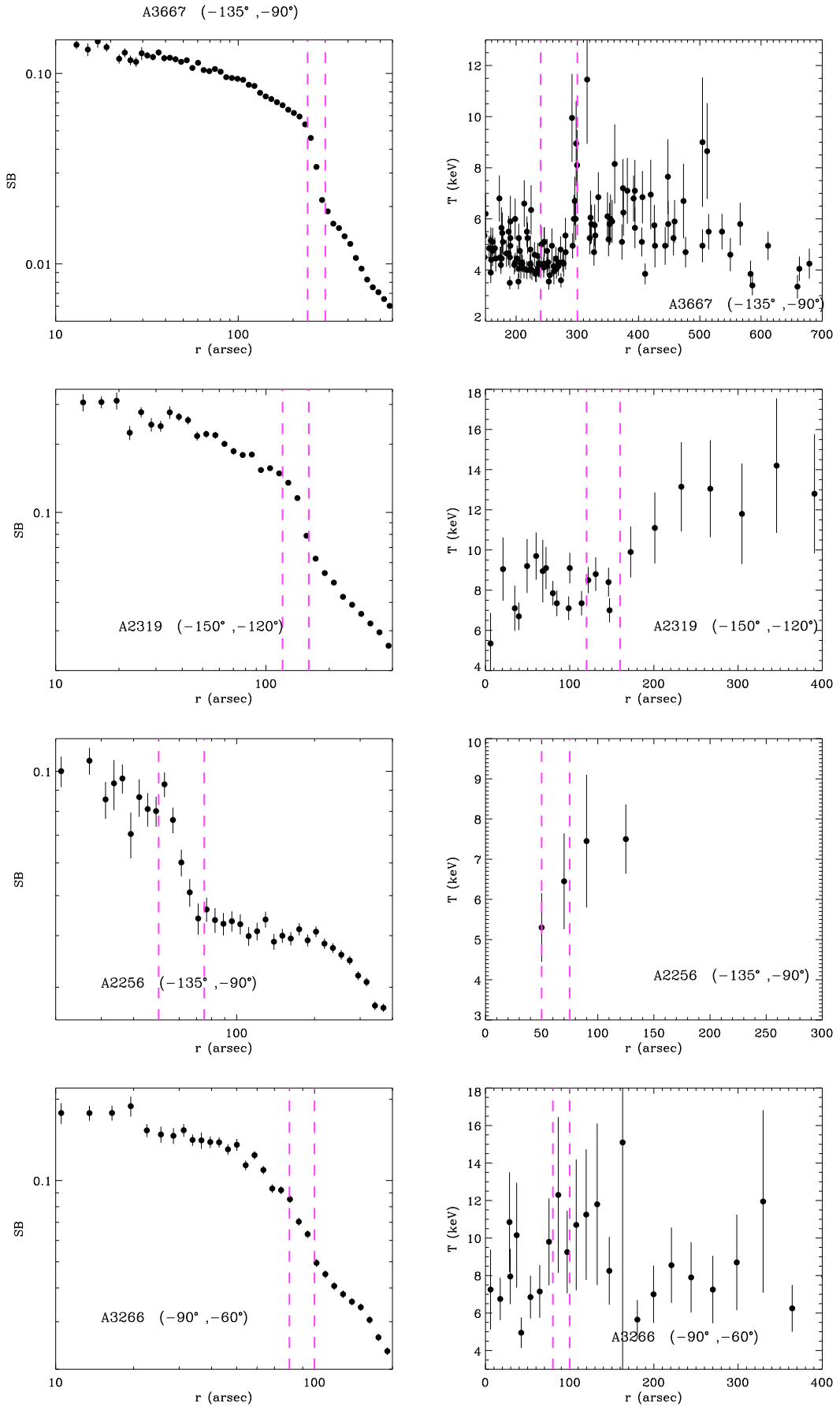


Fig. A.11. Surface brightness and temperature profiles for the cold fronts in A3667, A2319, A2256, and A3266.